⟩

# Further Investigations of
# Adaptive-Wall Wind Tunnels

J. C. Erickson, Jr., C. E. Wittliff, and D. C. Daughtry
Calspan Advanced Technology Center
Buffalo, New York 14225

October 1980

Final Report for Period August 1978 — December 1979

**ARNOLD ENGINEERING DEVELOPMENT CENTER**
**ARNOLD AIR FORCE STATION, TENNESSEE**
**AIR FORCE SYSTEMS COMMAND**
**UNITED STATES AIR FORCE**

This report has been reviewed by the Office of Public Affairs (PA) and is releasable to the National Technical Information Service (NTIS). At NTIS, it will be available to the general public, including foreign nations.

## APPROVAL STATEMENT

This report has been reviewed and approved.


ALEXANDER F. MONEY
Project Manager
Directorate of Technology


Approved for publication:

FOR THE COMMANDER


MARION L. LASTER
Director of Technology
Deputy for Operations

# UNCLASSIFIED

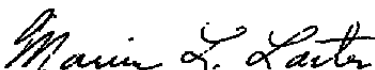| REPORT DOCUMENTATION PAGE | | READ INSTRUCTIONS BEFORE COMPLETING FORM |
|---|---|---|
| 1 REPORT NUMBER<br>AEDC-TR-80-34 | 2 GOVT ACCESSION NO. | 3. RECIPIENT'S CATALOG NUMBER |
| 4. TITLE (and Subtitle)<br>FURTHER INVESTIGATIONS OF ADAPTIVE-WALL WIND TUNNELS | | 5 TYPE OF REPORT & PERIOD COVERED<br>Final Report – August 1978 to December 1979 |
| | | 6 PERFORMING ORG. REPORT NUMBER<br>6374-A-1 |
| 7. AUTHOR(s)<br>J. C. Erickson, Jr., C. E. Wittliff and D. C. Daughtry | | 8 CONTRACT OR GRANT NUMBER(s)<br>F40600-78-C-0003 |
| 9 PERFORMING ORGANIZATION NAME AND ADDRESS<br>Calspan Advanced Technology Center<br>P. O. Box 400<br>Buffalo, New York 14225 | | 10. PROGRAM ELEMENT, PROJECT, TASK AREA & WORK UNIT NUMBERS<br>Program Element 65807F |
| 11. CONTROLLING OFFICE NAME AND ADDRESS<br>Arnold Engineering Development Center/DOS<br>Air Force Systems Command<br>Arnold Air Force Station, Tennessee 37389 | | 12 REPORT DATE<br>October 1980 |
| | | 13 NUMBER OF PAGES<br>70 |
| 14 MONITORING AGENCY NAME & ADDRESS(if different from Controlling Office) | | 15. SECURITY CLASS. (of this report)<br>UNCLASSIFIED |
| | | 15a. DECLASSIFICATION/DOWNGRADING SCHEDULE<br>N/A |

16 DISTRIBUTION STATEMENT (of this Report)

Approved for public release; distribution unlimited.

17 DISTRIBUTION STATEMENT (of the abstract entered in Block 20, if different from Report)

18 SUPPLEMENTARY NOTES

Available in Defense Technical Information Center (DTIC).

19. KEY WORDS (Continue on reverse side if necessary and identify by block number)

wind tunnels      static pipe
wall interference
adaptive-wall
self-correcting
transonic flow

20 ABSTRACT (Continue on reverse side if necessary and identify by block number)

The objective of this investigation was to continue the assessment of the Calspan perforated-wall, segmented-plenum adaptive-wall wind tunnel for flows in which the tunnel walls are supercritical. An important aspect of the investigation was the development of a static-pipe measuring technique for determining the normal velocity distributions. This technique was developed to overcome the limitations on the number of flow-angle probe measurements that could be made in the Calspan tunnel. The flow about a static pipe in the

DD FORM 1473 1 JAN 73    EDITION OF 1 NOV 65 IS OBSOLETE

# UNCLASSIFIED

20. ABSTRACT, Concluded.

presence of model/wall-induced disturbances was analyzed within the framework of slender-body theory to give the relationship between differential pressure measurements across the pipe and the steam-wise derivative of the normal velocity at the pipe centerline. Experiments with a 4% blockage NACA 0012 airfoil model at $M_\infty = 0.8$ and $\alpha = 4^\circ$ demonstrated that suitably constructed static pipes, in conjunction with several flow-angle probes, provide an improved technique for measuring the normal velocity distributions. Two converging iterative steps toward unconfined flow were accomplished at this test condition and established a basis for plenum-pressure control valve settings at thigher Mach numbers. In order to examine a case in which shock waves extend to the walls, the Mach number was increased to $M_\infty = 0.9$, with the model still at $\alpha = 4^\circ$. In the initial tests at this condition, the flow in the test section was choked downstream of the model. However, with increased suction just upstream of the model, the choking was relieved and adjustment of the flow to a reasonable first interative step was accomplished. Sufficient control appears to be available to continue interation toward unconfined flow for this case.

PREFACE


The work reported herein was conducted by Calspan Corporation for the
Department of the Air Force at the request of Headquarters, Arnold Engineering
Development Center/DOT, Arnold Air Force Station, Tennessee, under Contract
Number F40600-78-C-0003. Air Force technical representatives were Mr. E. R.
Thompson and Mr. A. E. Money. The investigation was conducted in the Aerodynamic
Research Department of the Calspan Advanced Technology Center, Buffalo, New York,
under the management of Dr. John C. Erickson, Jr.

The reproducibles used for this report were supplied by the authors,
J. C. Erickson, Jr., C. E. Wittliff and C. C. Daughtry. Appendix A.1 was
prepared by Dr. J. P. Nenni of Calspan ATC on the basis of his static-pipe
analysis by matched asymptotic expansions. The authors wish to acknowledge
the contributions by Professor W. R. Sears of the University of Arizona, a
consultant to Calspan, as well as by Calspan personnel Dr. A. Ritter, J. Nemeth,
R. E. Phibbs and the late A. F. Gretch.

TABLE OF CONTENTS

ILLUSTRATIONS

APPENDIX

1.0 INTRODUCTION

The influence of wall-interference effects on models tested in transonic wind tunnels has been an open question for many years, and it is generally acknowledged that many questions remain unanswered today. The accepted procedure has been to restrict the model size to be tested and to neglect the presumably small residual interference. However, recent requirements have led to testing larger models at high lift, while stressing extreme data accuracy. This gave renewed interest to methods for treating the wall-interference problem.

This state of affairs has led to the concept of an adaptive-wall wind tunnel in which the flow in the vicinity of the test-section walls is actively controlled in order to minimize or eliminate wall interference. The distributions of the disturbance velocity components are measured at discrete points along an imaginary control surface in the flow field near the walls, but away from the model. A theoretical formulation for the flow exterior to this control surface, including the unconfined-flow boundary condition that all disturbances vanish at infinity, is used to establish the functional relationships which must be satisfied at the control surface by the measured disturbance velocities. If the measured velocities do not satisfy these relationships, an iterative procedure provides a new approximation for the flow field at the surface, and the flow through the tunnel walls is readjusted until the measured quantities satisfy the functional relationships for unconfined flow. In this way, the best features of theory and experiment are combined to eliminate wall interference.

A program of research is in progress at Calspan Corporation to develop and demonstrate the feasibility of the adaptive-wall concept. This concept was described in general[1] and was demonstrated theoretically[2] in

---

1. Sears, W.R. "Self-Correcting Wind Tunnels" (The Sixteenth Lanchester Memorial Lecture.) The Aeronautical Journal, Vol. 78, No. 758/759, February/March 1974, pp. 80-89.

2. Erickson, J.C., Jr., and Nenni, J.P. "A Numerical Demonstration of the Establishment of Unconfined-Flow Conditions in a Self-Correcting Wind Tunnel" Calspan Report No. RK-5070-A-1, November 1973.

two-dimensional incompressible flow.   A two-dimensional adaptive-wall test section was designed, fabricated and installed in the circuit of the Calspan One-Foot Transonic Wind Tunnel.   The test section[3-4] consists of perforated upper and lower walls with segmented plenum chambers, each of which has an individual pressure control.   A model with an NACA 0012 airfoil section and a 6-inch chord was fabricated and tested[5] in the Calspan Eight-Foot Transonic Wind Tunnel to establish the airfoil characteristics in unconfined flow at a Reynolds number of $1.0 \times 10^6$ based on chord length.   Data were obtained over a Mach number range from 0.40 to 0.95 for an angle-of-attack range from -2° to 8°. An experimental demonstration of the tunnel in adaptive-wall operation was accomplished[3-4] for flows which were supercritical at the model but subcritical at the control surfaces and walls.

Upon completion of those experiments, research was initiated at Calspan, with AEDC sponsorship,[6] to extend the experiments to conditions where there is supercritical flow at the control surfaces and at the tunnel walls.   The present investigation continues the research along these lines and comprises one aspect of an overall theoretical and experimental AEDC effort on transonic adaptive-wall wind tunnel development.   The overall effort includes theoretical studies of the convergence aspects of adaptive-wall wind tunnels,[7,8] two-dimensional

3.     Vidal, R.J., Erickson, J.C., Jr., and Catlin, P.A.  "Experiments With a Self-Correcting Wind Tunnel" AGARD CP No. 174 on Wind Tunnel Design and Testing Techniques,  October 1975.

4.     Sears, W.R., Vidal, R.J., Erickson, J.C., Jr., and Ritter, A.  "Interference-Free Wind-Tunnel Flows by Adaptive-Wall Technology" Journal of Aircraft,  Vol. 14,  No. 11,  November 1977,  pp. 1042-1050.

5.     Vidal, R.J., Catlin, P.A. and Chudyk, D.W.  "Two-Dimensional Subsonic Experiments with an NACA 0012 Airfoil" Calspan Report No. RK-5070-A-3, December 1973.

6.     Vidal, R.J., and Erickson, J.C., Jr.  "Research on Adaptive Wall Wind Tunnels",  AEDC Report No. AEDC-TR-78-36,  November 1978.

7.     Lo, C.F. and Kraft, E.M.  "Convergence of the Adaptive-Wall Wind Tunnel" AIAA Journal, Vol. 16, No. 1, January 1978, pp. 67-72.

8.     Lo, C.F. and Sickles, W.L.  "Analytic and Numerical Investigation of the Convergence of the Adaptive-Wall Concept" AEDC Report No. AEDC-TR-79-55, November 1979.

adaptive-wall experiments in the Aerodynamic Wind Tunnel (1T) at AEDC to reduce wall interference by means of two different porous wall configurations,[9] and an application of the adaptive-wall concept in three-dimensional experiments with a swept-wing/body/horizontal-tail configuration in the Aerodynamic Wind Tunnel (4T) at AEDC wherein wall porosity is constant over each wall, but can vary from wall to wall.[10] An additional aspect of the overall AEDC program is the development of a computer code to model the inviscid, full-potential flow over three-dimensional swept wings in an adaptive-wall transonic wind tunnel.[11]

The results of the initial Calspan investigation for AEDC are described in detail in Reference 6. However, to provide continuity with the present study, the results of that program are summarized briefly here. The initial experiments with the 6-inch (6%-blockage) model were devoted to determining a practical mode of operation when shock waves from the model extend to the walls. This was necessary because the previously established operational mode for subcritical walls produced choked flow at and downstream of the model. The most practical mode of operation which resulted from the initial experiments consisted of two steps. First, wall control was used to obtain the desired distributions of the streamwise velocity component for a subcritical-wall case. Then, the Mach number was increased and the wall control was readjusted, sequentially, until the desired supercritical-wall test condition was achieved. At the high Mach numbers of interest, however, the available wall control was limited locally, and changes were required in the experimental apparatus.

---

9.  Kraft, E.M. and Parker, R.L., Jr. "Experiments for the Reduction of Wind Tunnel Wall Interference by Adaptive-Wall Technology" AEDC Report No. AEDC-TR-79-51, October 1979.

10. Parker, R.L., Jr. and Sickles, W.L. "Application of Adaptive Wall Techniques in a Three-Dimensional Wind Tunnel with Variable Wall Porosity" AIAA Paper No. 80-0157, January 14-16, 1980.

11. Mercer, J.E., Geller, E.W., Johnson, M.L. and Jameson, A. "A Computer Code to Model Swept Wings in an Adaptive Wall Transonic Wind Tunnel" AIAA Paper No. 80-0156, January 14-16, 1980.

A method was developed for analyzing and estimating flow-control requirements for adaptive-wall wind tunnels with perforated walls and segmented plenum chambers. The analysis treats the auxiliary compressor circuit for wall control and provides an approximate method for examining the trade-offs between the compression ratio of the auxiliary compressor, wall open-area ratio, and model size. For the purposes of the previous study, the most expeditious alternative for extending the operating range of the Calspan tunnel was to reduce model size by fabricating a 4-inch chord (4%-blockage) NACA 0012 airfoil model.

Iteration experiments with the 4%-blockage model at $M_\infty$ = 0.85 and $\alpha$ = 1° were performed. They were inconclusive because of flow-field unsteadiness. Wall control was used to obtain a first iterative step toward unconfined flow, but the shock wave on the lower surface fluctuated over about 15% of the chord. Subsequent attempts to iterate at this test condition did not lead to a steady flow field, and it was concluded that this test condition was not suitable for iteration at this stage of the tunnel development. Next, experiments were performed with the 4%-blockage model at $M_\infty$ = 0.8 and $\alpha$ = 4°, for which there is no shock wave on the lower airfoil surface and the upper shock should extend almost to the static pipe. Iterations in this case exhibited steady flow at each step, but a convergence anomaly occurred. That is, the third iterative step had almost converged, but the fourth appeared to diverge. In all of these experiments, the lack of a sufficient number of reliable normal velocity measurements at the control surfaces hindered the iterative process.

The objectives of the present investigation, then, were to continue the assessment of the Calspan two-dimensional, perforated-wall, segmented-plenum implementation of the adaptive-wall concept at supercritical-flow conditions for which model-induced shock waves reach the walls. An important aspect of the investigation was the development of a new instrumentation technique for determining the normal velocity component. This technique involves measurement of the static pressure at diametrically opposed orifices on the top and

.

bottom of a static pipe and relating the resulting distributions of the pressure differences to the streamwise derivative of the normal velocity. Details of the flow-measuring characteristics of the modified instrumentation and the implications on tunnel operation and data reduction procedures are described in Section 2. The experimental results are given in Section 3 beginning with calibrations of the instrumentation without the model present in the tunnel. Next, experiments with the 4%-blockage model at $M_\infty$ = 0.8 and $\alpha$ = 4° are reported, followed by the results of experiments with the same model at $M_\infty$ = 0.9 and $\alpha$ = 4°. In the latter case, the shock waves extend from the model to both walls. The investigation is summarized by concluding remarks in Section 4. In the Appendix, additional aspects of static-pipe technique are presented, namely an alternative derivation of the static-pipe characteristics to verify the completeness of the analysis, and some possible alternative implementations in both two- and three-dimensional flow fields.

## 2.0 INSTRUMENTATION

### 2.1 BACKGROUND

In the experiments prior to this investigation,[3,4,6] local flow angle was measured by aerodynamic probes and the local static pressure by static pipes. These measurements were used, respectively, to determine the normal, $v$, and streamwise, $u$, disturbance velocity components directly. However, the flow-angle measurements always limited the efforts. The inherent limitations in the probe technique arise because of the small scale, since blockage considerations limit the number of probes that can be used. Therefore, it is difficult to obtain sufficient measurements to define adequately the $v$ distributions. More-over, the small probes that must be used are very sensitive to contamination from oil present in the air stream of the tunnel. An alternative technique is to measure the static pressures at one control surface and the difference between those pressures and the pressures at a second surface slightly farther away from the model. In effect, this can be regarded as measuring the local static pressure and its gradient, from which the streamwise derivative of the normal velocity can be inferred. The advantage in this measurement technique is that static pressure is easy to measure with good precision and one can easily obtain good spatial resolution. The TSFOIL computer code[12] was used to calculate preliminary estimates of the pressure differences to be expected, and they are readily measurable in the immediate vicinity of the airfoil.

12.   Murman, E.M., Bailey, F.R. and Johnson, M.L.   "TSFOIL-A Computer Code for Two-Dimensional Transonic Calculations,  Including Wind-Tunnel Wall Effects and Wave-Drag Evaluation"  Paper No. 26 in Aerodynamic Analyses Requiring Advanced Computers,  NASA-SP-347-Part 2,  March 1975.

## 2.2    CONFIGURATION OF NEW INSTRUMENTATION

Several candidate static-pipe configurations for obtaining these differential measurements were examined. On the basis of available materials and ease of construction, it was decided that the new pipes would have a 5/8-inch OD circular cross section with diametrically opposed orifices on the top and bottom of the pipes in the vicinity of the model. There are 18 pairs of these orifices extending 9 inches upstream and 11 inches downstream of the junction between plenum chambers 6 and 7, as shown in Figure 1. These dual orifices span the region where the static pressure differences are equal to or greater than the resolution capability. Upstream and downstream of this region the static pipes have orifices which extend the full length of the test section along the side of the pipe facing the model. The most forward static pressure orifice on each pipe is connected to a manifold and the reading is taken to be the free-stream static pressure, $p_\infty$ . All remaining 33 pressures on the model sides of the pipes are measured relative to $p_\infty$ . In addition, the differential pressures between the 18 opposing pairs of orifices on each pipe are measured. The differential pressure transducers used have a probable error of 0.001 psi or less, and the read-out system has a resolution of 0.001 psi.

After fabrication, the new static pipes were mounted with their centerlines nominally four inches from the test section centerline, as the original pipes were. However, in order to use the probe flow-angle data in conjunction with the differential pressure data (as will be discussed in the next section), the probes were relocated to the plane of the static pipe centerlines from their original locations four and one-half inches from the test section centerline. In the original configuration, four of the probes in the vicinity of the model were mounted through the test windows and their frames. It was not feasible to relocate or remove these probes so they were retracted to lie against the side walls. However, two new flow-angle probes were fabricated and mounted in the vicinity of the model. The resulting locations of the flow-angle probes at the lower control surface are shown in the side view of Figure 1, while the upper probes are shown in the top planform view. The lateral staggering of the probes was chosen to avoid interference effects.

2.3    STATIC-PIPE ANALYSIS

The new static pipes are used to determine both disturbance velocity
components. The static pressures on the top and bottom of each pipe at a
given streamwise station are measured and averaged to infer the streamwise
disturbance velocity component at the control surface. In addition, the dif-
ference in pressure across the pipe can be used to infer the streamwise
gradient of the normal velocity component at the control surface. In the
following paragraphs the interaction between the flow to be measured and the
pipe is analyzed.

A schematic of the model and the upper pipe is shown in Figure 2.
The $x$-$y$ coordinate system in Figure 2 is used in the experiments as well as
in the analysis. The origin is at the tunnel centerline and the $y$ axis co-
incides with the vertical line passing through the junctions between plenum
chambers 6 and 7 and plenum chambers 16 and 17, see Figure 1. With the models
installed, the origin is 0.250$c$ behind the leading edge of the 6%-blockage
model and 0.175$c$ behind the leading edge of the 4%-blockage model when the
models are at zero angle of attack.

The nose of the pipe is located well upstream of the test section
in the contraction region. Therefore, the pipe can be considered to be doubly
infinite in length and of constant radius, $R$ , so far as the flow analysis is
concerned. The flow in the vicinity of the pipe is assumed to be inviscid
and irrotational and to consist of perturbations about a free stream of speed
$U_\infty$ . Accordingly, a perturbation velocity potential, $\phi$ , exists and will be
written as

$$\phi(x,y,z) = \phi^m(x,y) + \phi^p(x,y,z) \qquad (1)$$

where $\phi^m(x,y)$ is the two-dimensional potential of the disturbances introduced
by the model, including its interaction with the wall, and $\phi^p(x,y,z)$ is
the three-dimensional potential of the disturbances arising from the inter-
action of the pipe with the model/wall flow field. The objective of the

analysis is to determine $\phi$ and its derivatives on the pipe in terms of the model/wall-induced flow field that is to be determined, namely $\phi^m$ and its derivatives. The disturbances introduced by the model and wall are assumed to be of order of magnitude $\epsilon$, which represents the thickness ratio, $\tau$, or angle of attack, $\alpha$, of the model. The characteristic length of the model/wall flow field is the airfoil chord, $c$, and therefore a small parameter representing the pipe flow field is $\delta = R/c$. Both $\epsilon$ and $\delta$ are of the same order of magnitude so the analysis must be carried out to include terms of order $\epsilon^2$, $\delta^2$ and $\epsilon\delta$.

The doubly-infinite static pipe is as shown in Figure 3. The coordinates are the same as in Figure 2, except for a transformation to the pipe centerline,

$$y' = y - h_o \qquad (2)$$

The model/wall-induced velocity components along the pipe centerlines, $u_o$ and $v_o$, are given by

$$u_o(x) = [\partial \phi^m / \partial x]_{y'=0} \qquad (3)$$

$$v_o(x) = [\partial \phi^m / \partial y']_{y'=0} \qquad (4)$$

The superscript $m$ has been omitted from $u_o$ and $v_o$ to simplify the notation, since these are the quantities to be deduced from the pipe measurements. Although the normal component $v^m$ varies with $y'$ over the pipe, this effect is of higher order and so $v_o(x)$ can be considered as the incident velocity normal to the pipe, as shown in Figure 3. Since the pipe is assumed doubly infinite in length, the streamwise perturbation $u^m$ does not interact with the pipe although its variation with $y'$ is taken into account as described below. Since typical maximum values of $v_o(x)$ correspond to an angle of only a few degrees, it is satisfactory to use Munk-Jones theory for the attached flow over slender bodies at an angle of attack.[13] The analysis given below is cast in terms of conventional slender-body theory. However, a more rigorous

---

13. Sears, W.R. "Small Perturbation Theory", Section C of General Theory of High Speed Aerodynamics, Vol. VI of High Speed Aerodynamics and Jet Propulsion, Princeton U. Press, 1954.

analysis using matched asymptotic expansions is presented in Appendix A.1. This latter analysis verifies that the results obtained are correct to second order.

Application of Munk-Jones theory to this compressible-flow configuration gives the perturbation potential for the pipe as simply that for a doublet in incompressible crossflow of strength $v_o(x)$, namely

$$\phi^P(x, y, z) = -v_o(x) R^2 \cos \omega / r \tag{5}$$

where the cylindrical coordinates of Figure 3 are used for convenience. This is the potential necessary to insure zero normal flow at the pipe surface for the incident crossflow $v_o(x)$. The velocity components corresponding to $\phi^P$ for an arbitrary field point, again in cylindrical coordinates, are

$$v_x^P(x, r, \omega) = -v_o'(x) R^2 \cos \omega / r \tag{6}$$

$$v_r^P(x, r, \omega) = v_o(x) R^2 \cos \omega / r^2 \tag{7}$$

$$v_\omega^P(x, r, \omega) = v_o(x) R^2 \sin \omega / r^2 \tag{8}$$

where $v_o'(x) = d\, v_o(x)/dx$. When these are resolved into the $x$, $y$, $z$ coordinates, they become

$$u^P(x, r, \omega) = -v_o'(x) R^2 \cos \omega / r \tag{9}$$

$$v^P(x, r, \omega) = -v_o(x) R^2 \cos 2\omega / r^2 \tag{10}$$

$$w^P(x, r, \omega) = -v_o(x) R^2 \sin 2\omega / r^2 \tag{11}$$

When these expressions are evaluated on the pipe, $r = R$, and are added to the velocity components of the model/wall-induced flow field,

the total perturbation velocities $u$, $v$, $w$ on the pipe are obtained. Treating the streamwise component first, it follows that

$$u = u^m(x, y') + u^p(x, R, \omega) \tag{12}$$

On the pipe $u^m$ varies with $y'$ and the first two terms of a Taylor's series can be written as

$$u^m(x, y') = u_o(x) + [\partial u^m / \partial y']_{y'=0} \, y' \tag{13}$$

where the terms neglected are of order $\epsilon \delta^2$. If the equation

$$y' = y - h_o = -R \cos \omega \tag{14}$$

which holds on the pipe, is used with the condition for irrotational flow

$$[\partial u^m / \partial y']_{y'=0} = v_o'(x) \tag{15}$$

it follows that

$$u^m(x, y' = -R\cos\omega) = u_o(x) - v_o'(x) R \cos \omega \tag{16}$$

When this is added to Eq. (9), the result on the pipe is

$$u = u_o(x) - 2 v_o'(x) R \cos \omega \tag{17}$$

where the second term has equal contributions from the $y$-derivative of the model/wall-induced flow at the pipe and from the crossflow-induced flow over the pipe. Since $u_o(x)$ is of order $\epsilon$, and $R v_o'(x)$ is of order $\epsilon\delta$, the terms in Eq. (17) are of first order and second order, respectively. The components $v$ and $w$ on the pipe follow directly from Eqs. (10) and (11) and the fact that for two-dimensional flows $w_o(x) = 0$, namely

$$v = v_o(x) - v_o(x) \cos 2\omega \tag{18}$$

$$w = -v_o(x) \sin 2\omega \tag{19}$$

The exact pressure coefficient for isentropic flow, when expanded to second order in the perturbation velocity components, is

$$C_p = -2(u/U_\infty) - \beta^2(u/U_\infty)^2 - [(v/U_\infty)^2 + (w/U_\infty)^2] \quad (20)$$

where $\beta^2 = 1 - M_\infty^2$. It is convenient at this point to nondimensionalize according to $(\hat{\ }) = (\ )/U_\infty$ and $\bar{z} = z/c$. Then, substitution of Eqs. (17) to (19) into Eq. (20) and retention of all second-order terms in $\epsilon$ and $\delta$ give for the pressure coefficient on the pipe,

$$C_p(\bar{z}, \omega) = -2\hat{u}_o(\bar{z}) + 4\delta\,\hat{v}_o'(\bar{z})\cos\omega - \beta^2\hat{u}_o^2(\bar{z})$$
$$- 4\,\hat{v}_o^2(\bar{z})\sin^2\omega \quad (21)$$

Therefore, the objective of the analysis has been achieved by relating the pressure coefficient measured on the pipe to the model/wall-induced velocity components $\hat{u}_o$ and $\hat{v}_o$ at the pipe centerline.

The static pipes used in the earlier experiments[3,4,6] had a single row of orifices at $\omega = \pi/2$, so

$$C_{p_o} \equiv C_p(\bar{z}, \pi/2) = -2\hat{u}_o(\bar{z}) - \beta^2\hat{u}_o^2(\bar{z}) - 4\,\hat{v}_o^2(\bar{z}) \quad (22)$$

In the earlier experiments, this expression was approximated by the leading, first-order term in order to evaluate $\hat{u}_o(\bar{z})$ from the $C_{p_o}$ measurements. This linearization was consistent with the external-flow calculations for unconfined flow since they are based upon transonic small-disturbance theory.

The new static pipes have two rows of orifices located at $\omega = 0$ and $\pi$ ($y = h_1$ and $h_2$ in Figure 3), for which Eq. (21) gives

$$C_{p_1} = C_p(\bar{z}, 0) = -2\hat{u}_o(\bar{z}) + 4\delta\,\hat{v}_o'(\bar{z}) - \beta^2\hat{u}_o^2(\bar{z}) \quad (23)$$

$$C_{p_2} \equiv C_p(\bar{z}, \pi) = -2\hat{u}_o(\bar{z}) - 4\delta\,\hat{v}_o'(\bar{z}) - \beta^2\hat{u}_o^2(\bar{z}) \quad (24)$$

If these are added and rearranged, it follows that

$$\hat{u}_o(\bar{z}) + \frac{\beta^2\hat{u}_o^2(\bar{z})}{2} = -\frac{C_{p_1} + C_{p_2}}{4} \quad (25)$$

which can be solved to obtain

$$\hat{u}_o(\bar{x}) = -\frac{1}{\beta^2}\left\{1 - \left[1 - \frac{\beta^2(C_{P_1} + C_{P_2})}{2}\right]^{1/2}\right\} \qquad (26)$$

which reduces to the linear relationship

$$\hat{u}_o(\bar{x}) = -\frac{C_{P_1} + C_{P_2}}{4} \qquad (27)$$

for small disturbances. If Eqs. (23) and (24) are subtracted and rearranged, it follows that

$$\hat{v}_o'(\bar{x}) = \frac{C_{P_1} - C_{P_2}}{8\delta} \qquad (28)$$

The result emphasizes the importance of accounting properly for the interaction between the pipe and the model/wall flow field. If that interaction were ignored and only the variation of $u^m$ with $y'$ considered, the factor of 8 in the denominator would be reduced to 4, so a totally incorrect result would have been obtained.

The $\hat{v}_o(\bar{x})$ distribution over the interval of the static pipe differential measurements is found by integration, namely

$$\hat{v}_o(\bar{x}) = \hat{v}_o(\bar{x}_o) + \int_{\bar{x}_o}^{\bar{x}} \left[\hat{v}_o'(\xi)\right] d\xi \qquad (29)$$

where $\hat{v}_o'(\xi)$ is given by Eq. (28) and $\hat{v}_o(\bar{x}_o)$ is the value of $\hat{v}_o$ at some reference point $\bar{x}_o$. The probe measurements are used to determine $\hat{v}_o(\bar{x}_o)$, as well as to complete the determination of the $\hat{v}_o$ distribution upstream and downstream of the limits of the $C_{P_1} - C_{P_2}$ measurements. This combination of probe and pressure gradient measurements provides the $\hat{v}_o$ distributions which are used as the boundary conditions for the external-flow calculations.

The analysis given here for the flow about the static pipe is no longer valid in the immediate region where a shock wave from the model or wall impinges on the pipe. Accordingly, special treatment is necessary when this

occurs. The procedure for handling the data near shocks is described in Section 2.4, where results for a typical case are presented and discussed.

## 2.4   NORMAL-VELOCITY DATA PROCEDURE

In this section, the notation will be simplified from that of the analysis for use in the remainder of the report.  In particular, the subscript zero will be dropped from the disturbance velocity components $u_o$ and $v_o$ at the control surfaces and from the control surface location $h_o$ .  Thus $u$ and $v$ will refer to these components evaluated at the control surfaces located at $y = \pm h$  .

The data procedure is best described by considering an example.  The example chosen is the second step in the experimental iteration for $M_\infty = 0.8$ and $\alpha = 4°$ that is discussed in Section 3.2.  The data for $d\,(v/U_\infty)/d(x/c)$, as calculated by Eq. (28) from the static-pipe measurements, are presented in Figures 4a and 4b for the upper and lower control surfaces, respectively. The estimated unconfined-flow distributions calculated by TSFOIL are also given in Figure 4, but are for reference only since there is no reason to believe that the data at this step of the iteration should agree with the estimate.

The data procedure at the lower control surface will be discussed first since there was no shock wave below the airfoil.  The $d\,(v/U_\infty)/d(x/c)$ data of Figure 4b were fit by a cubic spline over the entire interval from $x/c = -2.25$ to $x/c = 2.75$ for which measurements were made.  This spline fit was then integrated according to Eq. (29) with the reference velocity $v\,(x_o/c)/U_\infty$ temporarily set equal to zero at  $x/c = -2.25$ to give the dashed curve shown in Figure 5b.  The actual reference velocity $v\,(x_o/c)/U_\infty$ was then established by a least-squares fit of the integrated curve to the four probe measurements of $v/U_\infty$ at  $x/c = -1.48$, $-1.12$, $0.83$ and $2.52$ in Figure 5b. The resulting curve was then faired upstream through the first three probe measurements and downstream through the last two to arrive at the final $v_m/U_\infty$ distribution shown in Figure 5b.

At the upper control surface the shock wave appears just to reach the upper pipe, as indicated by Schlieren observations. As shown in Figure 4a, there are very large gradients of $d(v/U_\infty)/d(x/c)$ in the vicinity of the shock. Unfortunately the spacing of the measurements is still large enough that the curve cannot be clearly resolved in this region. Therefore separate treatment is required upstream and downstream of the shock, whose location in any experiment is apparent from the $d(v/U_\infty)/d(x/c)$ data and the Schlieren observation. Accordingly, the $d(v/U_\infty)/d(x/c)$ data were fit by a cubic spline from the first measured point at $x/c = -2.25$ to the last point before the shock at $x/c = 0.25$. The spline fit was then integrated up to $x/c = 0.25$ with the reference velocity $v(x_s/c)/U_\infty$ temporarily set equal to zero at $x/c = -2.25$ to give the dashed curve in Figure 5a. The actual reference velocity was chosen by adjusting the integrated curve to pass through the probe measurement at $x/c = -1.95$ and the curve was faired upstream through the first two probe measurements. Downstream of the shock a similar procedure was used. The $d(v/U_\infty)/d(x/c)$ data from $x/c = 0.50$ to $x/c = 2.75$ were spline fit and then integrated upstream from a temporary reference value of zero at $x/c = 2.75$ to $x/c = 0.50$ to give the other branch of the dashed curve in Figure 5a. This branch was adjusted by a least-squares fit to the two probe measurements at $x/c = 1.25$ and $2.05$. It was then faired downstream through the last three probe measurements. In the vicinity of the shock, the upstream and downstream branches were simply extrapolated until they intersect to give the final $v_m/U_\infty$ distribution in Figure 5a.

It is clear that additional measurements in the vicinity of the shock wave would be highly desirable, but this was not possible with the present configuration. In fact, it would be difficult to construct a pipe with sufficient measurement orifices to cover all shock locations for a wide range of models and operating conditions. Accordingly, an alternative such as pipes which translate streamwise offers a better possibility for more complete definition of the distributions in future applications. Despite this limitation of the existing configuration, the new static pipes, in conjunction with the probes, provide an improved technique for determining the normal-velocity distributions compared to that of the probes alone.

21

## 2.5   ADAPTIVE-WALL OPERATING TECHNIQUE

The adaptive-wall operating technique is basically the same as that used in the past,[3-4] with data procedures modified to suit the new static-pipe configuration. An initial approximation to the static pressure distributions on the pipes, $C_{P_1}^{(1)}$ say, is found by using TSFOIL to estimate the unconfined-flow distributions of $u/U_\infty$ and $d(v/U_\infty)/d(x/c)$ for use in evaluating Eq. (23). The resulting $C_{P_1}^{(1)}$ distributions are set in the tunnel and the $C_{P_1}^{(1)} - C_{P_2}^{(1)}$ distributions are measured along with the probe readings. From these measurements, the actual experimental distributions $v^{(1)}/U_\infty$ are evaluated as described above and used as boundary conditions for the external-flow calculation of the corresponding unconfined-flow distributions $u^{(2)}/U_\infty$. These calculations are made using a computer code based on finite-difference solutions to the transonic small-disturbance equations. This code had been developed[4] and used[6] in the earlier investigations. The new calculated distributions $u^{(2)}/U_\infty$ are used, in turn, along with $d(v^{(1)}/U_\infty)/d(x/c)$ and Eq. (23) to determine calculated distributions, $C_{P_1}^{(ii)}$ say, which are relaxed to get the distributions to be set in the tunnel in the second iterative step, namely

$$C_{P_1}^{(2)} = (1 - k) C_{P_1}^{(1)} + k\, C_{P_1}^{(ii)} \tag{30}$$

where $k$ is the relaxation factor. After setting $C_{P_1}^{(2)}$, the appropriate measurements are repeated and the iteration continued until convergence is achieved.

# 3.0 EXPERIMENTS

## 3.1 INSTRUMENTATION CALIBRATIONS

The first experiments were a series of tests without the airfoil
model installed in the tunnel. For convenience, these will be referred to as
empty-tunnel tests. These tests were necessary in order to calibrate the two
new flow-angle probes over the geometric angle-of-attack range from -4° to
+4° at free-stream Mach numbers from 0.55 to 0.95. It was found that the
response of the new probes to changes in angle of attack is linear, which is
in agreement with the response of the other flow-angle probes. These experi-
ments also were required to provide new probe readings at zero flow angle over
the same Mach number range, since all the probes had been relocated in the
plane of the static-pipe centerlines. Later, during the course of the itera-
tion experiments, additional empty-tunnel runs were made to acquire updated
flow-angle probe calibrations at zero angle of attack.

As a by-product of these empty-tunnel calibrations runs, the quality
of the uniform flow in the test section was measured. Typical results at
$M_\infty = 0.85$ are shown in Figure 6 and compared with earlier data obtained with
the original 1/2-inch OD static pipes. The results are presented as the stream-
wise disturbance velocity component $u/U_\infty$ plotted as a function of the distance
from the beginning of the controlled part of the test section. The quality of
the uniform flow obtained in the recent tests matches that of the earlier
results. Any variations in velocity exceeding 0.5% occur either near the begin-
ning of the test section, or well downstream near the end of the test section.
For the data shown in Figure 6, the mean values of $u/U_\infty$ are -0.0008 and -0.0009
for the present and previous tests, respectively. The corresponding standard
deviations for both sets of data are $\pm 0.0024$.

The new static pipe data have been analyzed for each of the test
Mach numbers. The mean values of $u/U_\infty$ and the standard deviations are pre-
sented in Table I for representative cases. The deviation of the mean values

23

from zero is significantly less than the standard deviations (with one exception - the upper pipe at $M_\infty$ = 0.55). The flow quality at Mach numbers of 0.55, 0.75 and 0.85 is comparable and the standard deviations are all about ±0.0020. At $M_\infty$ = 0.95, the standard deviation of all the data is approximately ±0.0040; however, this is due to deviations at the far upstream and downstream ends of the test section. Over the central 20-inch distance near the model location, the standard deviation is ±0.0022, which is in good agreement with the lower Mach number results.

The pressure differentials measured by the opposing pairs of orifices have also been analyzed. The mean values, expressed as $C_{P_1} - C_{P_2}$ , and the standard deviations are shown in Table II for the same representative cases. These orifices, which are located as shown in Figure 1, exhibit mean values of about ±0.0010 with standard deviations of ±0.0020. These mean values are small and comparable to those for the overall flow, as in Table I and Figure 6. However, the fact that the means are not zero has a significant implication on the determination of $v/U_\infty$ with the pipes. The empty-tunnel differential pressure data were reduced, spline fit and integrated according to Eq. (29) over the total length of the measurements from $z/c$ = -2.25 to 2.75 using the standard data reduction procedure. The resulting cumulative effect of the nonzero pressure differentials of one predominant sign was very large. This can be seen in Figure 7, where the results at the upper pipe for two different empty-tunnel runs at $M_\infty$ = 0.8 are presented. Since this plot is to the same scale as Figure 5, a comparison shows just how large the effect is. All empty-tunnel data were examined in this way. It was found that the upper pipe data integrated in all cases to give positive $v/U_\infty$ distributions of roughly the magnitude shown in Figure 7. At the lower pipe, however, the results were different and contradictory. That is, some cases integrated to give positive $v/U_\infty$ (of smaller magnitude than in Figure 7) and some to give negative $v/U_\infty$. Indeed, at the lower pipe $v/U_\infty$ was positive in one run and negative in the other for the experiments shown in Figure 7.

Several possible causes of this phenomenon were examined. Calculations indicated that the pipe does not deflect statically an amount sufficient to cause distributions of $d(v/U_\infty)/d(x/c)$ of the magnitude that was measured. This was verified by careful measurements along the length of the pipes of the distance from the pipe to the wall. However, the deflection under tunnel operating conditions, including dynamic loads and thermal effects, could not be assessed readily. The normal velocities implied at both pipes by the measurements for each run can be interpreted in terms of an apparent effective area change in the flow. Such an area change implies a variation in $u/U_\infty$ along the streamwise direction by consideration of the continuity equation. For two representative cases, the implied $u/U_\infty$ distribution due to the $v/U_\infty$ measured at the two pipes was calculated by means of a one-dimensional flow model. The calculated $u/U_\infty$ values were very much larger in magnitude and varied with $x/c$ in an entirely different way from the measured $u/U_\infty$ values, e.g., those shown in Figure 6. Therefore it was concluded that the flow is in fact uniform, as indicated by the small measured $u/U_\infty$ variations, and the anomalies in the pipe differential measurements are an artifact of the detailed geometry of the individual pipes, since the characteristics of each differ. Consequently, this effect at the upper pipe was treated as a tare reading to be subtracted at each orifice from the measured $d(v/U_\infty)/d(x/c)$. The integrated $v/U_\infty$ from the assumed tare is shown in Figure 7 and appears to provide a reasonable approximation to the experimental curves for both empty-tunnel runs at this $M_\infty$. No tare was used at the lower pipe because it averaged nearly to zero for all runs considered.

3.2     EXPERIMENTS AT $M_\infty = 0.8$ AND $\alpha = 4°$                    .

These experiments with the 4%-blockage model were performed in order to investigate further the convergence anomaly that had been observed in the earlier experiments, as mentioned in the Introduction. Initially, this case was chosen because it provides a flow field in which only the upper airfoil surface is supercritical with the shock extending to the vicinity of the static pipe, but not to the wall. Rather than beginning where the earlier

experiments ended, it was more convenient with the new instrumentation to begin the iteration over. Accordingly the procedure outlined in Section 2.5 was used.

Some difficulty was encountered in eliminating an apparent cross-flow condition upstream of the model at the first three plenum chambers on the upper and lower walls. This same difficulty had occurred in the divergent fourth iterative step of the earlier investigation. It was found that this tendency could be avoided, or minimized, if the valve settings at the up-stream plenum chambers were set initially at the empty-tunnel settings for the same free-stream Mach number. Accordingly a reasonable first step in the iteration was set. The resulting pressure distribution on the airfoil was in only fair agreement with the Eight-Foot Tunnel data,[5] see Figure 8, with the shock too far back. It should be recalled, however, that the Eight-Foot Tunnel data were obtained at a Reynolds number of 1.0 x $10^6$ based on model chord while the present data with the 4%-blockage model correspond to a Reynolds number of 0.67 x $10^6$. Earlier experiments had shown in a short dura-tion run that at $M_\infty = 0.8$ and $\alpha = 4°$, the shock wave moved forward as the Reynolds number was increased from 0.67 x $10^6$ to 1.0 x $10^6$.

Although there seemed to be a slight residual negative crossflow upstream from the probe measurements, nevertheless the pipe differential-pres-sure and probe data were reduced as described in Section 2.4 to obtain the $v_m/U_\infty$ distributions to be used as boundary conditions for the external flow calculations. The resulting unconfined-flow distributions corresponding to $v_m/U_\infty$, $u[v_m/U_\infty]/U_\infty$, are compared with the measured distributions in Figure 9. There are significant differences between the distributions and they arise in part from the crossflow. Following the adaptive-wall iterative technique of Section 2.5, the $C_{p_i}^{(ii)}$ results corresponding to the computed values of Figure 9 were relaxed according to Eq. (30) with a relaxation factor of 0.1. That is, only very small changes from the initial settings were called for.

The crossflow disappeared while setting the second step in the iterative procedure. This can be seen from the $v_m/u_\infty$ distributions that were described in Section 2.4 and are shown in Figure 5. The pressure distribution on the airfoil, Figure 10, is greatly improved over that of the first iterative step in Figure 8, although the difference in Reynolds number still exists. Evaluation of the external-flow calculations using the $v_m/u_\infty$ distributions of Figure 5 yields the $u [v_m/u_\infty]/u_\infty$ distributions given in Figure 11. The agreement is much better than in the first iterative step, especially near the model but there are still appreciable differences upstream and downstream.

It was intended to iterate further by taking a third step, also with $k = 0.1$. At this time, however, an accident occurred while running the One-Foot Tunnel and severe overheating resulted. An upstream segment of the adaptive-wall test section was damaged and required rebuilding. Thus, the model and instrumentation had to be removed. After the repairs were effected and additional tunnel calibrations were carried out, the iterations could not be resumed easily from the point where they had ended. Nevertheless, the results of these two iterations established the new measurement technique and also provided a basis of valve settings for experiments at higher Mach numbers where both control surfaces are supercritical.

3.3     EXPERIMENTS AT $M_\infty$ = 0.9 AND $\alpha$ =4°

These experiments with the 4%-blockage model were performed to examine the control available when both walls are supercritical. Existing numerical results for the flow fields of the NACA 0012 section, as calculated by TSFOIL, were analyzed to select suitable cases. An additional constraint on the selection was the desire to choose an angle of attack sufficiently large to avoid the very small lift-curve slope that is characteristic of this airfoil at $M_\infty$ = 0.85 and 0.9 for angles of attack of three degrees or less, see Figure 5 of Reference 5 or Figure 3 of Reference 6. This apparently results from the shock-wave locations on the upper and lower control surfaces.

As had been observed in Reference 6, unsteady shock locations existed when the 4%-blockage model was tested in this range, namely at $M_\infty = 0.85$ and $\alpha = 1°$. Although it is not known if the small lift-curve slope and the unsteadiness are related, it was desired to avoid this angle-of-attack range for the next set of experiments. Selection of $M_\infty = 0.9$ and $\alpha = 4°$ satisfied the criteria for supercritical walls and a reasonable lift-curve slope.

In the TSFOIL calculations, the lift coefficient measured in the Eight-Foot Tunnel tests was specified instead of the Kutta condition at the trailing edge. This was done so that the peaks of the computed $u/U_\infty$ distributions and the computed distributions far upstream and downstream of the model would be representative of the actual experimental conditions for unconfined flow. The drawback of specifying the lift in this Mach number range is that there can be an appreciable flow around the trailing edge, which gives rise to obvious errors in the pressure distribution on the model. These errors are not of major concern, but in some examples, their effect does appear in the induced velocities at the control surfaces above and below the trailing edge. Therefore, the calculated TSFOIL distributions for $C_{p_1}^{(1)}$ were used only as a guide for setting the flow in the first iterative step and it was not required that they be set exactly. In subsequent iterative steps, of course, the measured distributions and the distributions from the external-flow calculations determine the next settings, according to Eq. (30).

In the initial experiments to set this flow field, most of the plenum-pressure control valves were opened to settings representative of the experiments at $M_\infty = 0.8$ and $\alpha = 4°$. This was in accordance with the procedure developed in Reference 6 for setting supercritical flows by proceeding upward in $M_\infty$ from a related subcritical case. However, the valves at the first three plenum chambers at the upper wall and the first two chambers at the lower wall were set at the empty-tunnel, uniform-flow settings for $M_\infty = 0.9$. As mentioned in Section 3.2 this procedure had been reasonably effective in eliminating crossflow upstream.

When the tunnel was run at these valve settings, considerable difficulty was encountered in reaching the desired free-stream Mach number. The required tunnel-drive power increased very rapidly and limited the achievable $M_\infty$ to about 0.89. Schlieren observations indicated that the shock waves on both airfoil surfaces were at the trailing edge and were steady. It was suspected that the tunnel was choked downstream of the model and this was verified by the $u_m/U_\infty$ measured at the static pipes and shown in Figure 12. These results are reminiscent of the first attempt to set supercritical flows in earlier experiments, see Figures 5 and 6 of Reference 6. That is, the $u_m/U_\infty$ distributions were reasonable upstream of the model, but the flow was supersonic downstream. It should be emphasized that no valve adjustments had been made at this point.

The second run began with the same valve settings and an $M_\infty$ of 0.89. Valve adjustments were then carried out. Increasing the suction at the upper plenum chamber just ahead of the model (plenum No. 6 in Figure 1) and the corresponding lower plenum chamber (plenum No. 16 in Figure 1) served to unchoke the flow. The power requirements immediately dropped significantly along with key tunnel-drive-system temperatures and the flow became noticeably quieter. The free-stream Mach number was increased to 0.9 without difficulty. The $u_m/U_\infty$ distributions were measured without further adjustments and are presented in Figure 13. The flow downstream of the model was mostly subcritical, but still far from that desired.

A third run was made in which additional valve adjustments were made in the usual fashion. Upstream of the model, the $C_{p_1}^{(1)}$ distributions were set closely to the TSFOIL values, but just downstream of the model they were not. It is in this neighborhood, however, where the TSFOIL results are questionable. The measured $u_m/U_\infty$ distributions are given in Figure 14 together with the $u[v_m/U_\infty]/U_\infty$ distributions calculated from the external flow. The large differences between $u_m/U_\infty$ and $u[v_m/U_\infty]/U_\infty$ at the upper control surface upstream and downstream of the model arise, in part at least, from appreciable scatter in the probe measurements beyond the interval where the static-pipe

differential pressure measurements are made. The scatter made interpolation difficult. The measured pressure distribution on the airfoil is compared with the Eight-Foot Tunnel data in Figure 15. The agreement is generally satisfactory although the upper-surface shock lies ahead of its unconfined-flow location and the pressure rise associated with the shock extends over a greater portion of the chord. The Reynolds number is still two-thirds of that for the Eight-Foot Tunnel experiments but its effect on the flow has not been established for these flow conditions. The results shown in Figure 14 provide the basis for a second iterative step according to Eq. (30), again with $\ell = 0.1$. Although subsequent iterative steps were not made for this case, sufficient wall control appears to be available to continue the iteration procedure.

## 4.0 CONCLUDING REMARKS

The purpose of this research was to continue the assessment of the Calspan adaptive-wall wind tunnel for two-dimensional flows with supercritical walls. An important aspect of the research was the investigation of a static-pipe measuring technique for determining the normal velocity distributions. This technique was developed to overcome the limitations in the number of flow-angle probe measurements that could be made in previous experiments.

The flow about static pipes in the presence of model/wall-induced disturbances was analyzed within the framework of conventional slender-body theory and the theory of matched asymptotic expansions. This analysis relates differential pressure measurements across the pipe to the streamwise derivative of the normal velocity at the pipe centerline. The derivative is integrated to obtain the distribution of the normal velocity if at least one independent normal velocity measurement is made. In addition, the average of the pressure measurements across the pipe determines the streamwise velocity component at the pipe centerline. Two suitable static pipes were constructed. For uniform, parallel flow in the empty test section, the differential pressure measurements indicated an apparent gradient in normal velocity at the upper pipe for all Mach numbers tested. It has been concluded that this gradient is an artifact of the pipe construction and installation. Accordingly, it has been eliminated by treating the empty-tunnel gradient as a tare reading. The new static-pipe technique, in conjunction with flow-angle probes, was applied to cases with a model present at $M_\infty$ = 0.8 and $\alpha$ = 4°. Results indicated that the procedure is an improvement over probes alone and it was used in the subsequent experiments. Also, static pipes can be used to determine the velocity normal to the pipe in three-dimensional model/wall-induced disturbance fields. However, further development to provide additional measurements in regions of large normal-velocity gradients should be carried out concurrently with analysis of the interaction between a shock wave and the static pipe.

A series of tunnel-empty runs in uniform, parallel flow served to calibrate the instrumentation over a range of Mach numbers. In addition, analysis of the results showed that the flow quality matched that of earlier experiments.

The 4%-blockage NACA 0012 airfoil model was run at $M_\infty = 0.8$ and $\alpha = 4°$, and two converging steps in an experimental iteration were accomplished. From runs made prior to beginning the actual iteration, it was concluded that cross-flow conditions upstream of the model could be minimized in the first iterative step by initiating the wall control adjustment with the upstream valves set at their tunnel-empty positions at that $M_\infty$. From these successful experiments, sufficient information was obtained to proceed to a flow with both walls supercritical. Accordingly, the same model was tested at the same $\alpha$, but with $M_\infty$ increased to 0.9.

Initial experiments at $M_\infty = 0.9$ and $\alpha = 4°$ were performed with the upstream control valves at their tunnel-empty settings and the remaining valves at their $M_\infty = 0.8$ and $\alpha = 4°$ settings. The measured streamwise velocity component at the control surfaces exhibited a reasonable distribution from the beginning of the test section to the vicinity of the airfoil trailing edge with these settings. Downstream of this point, however, the flow was choked and supersonic flow persisted to the end of the test section. The choking was relieved by increasing the suction at the upper and lower plenum chambers just upstream of the model. Further control adjustments led to reasonable streamwise velocity distributions along the entire length of the control surfaces. Therefore, a first iterative step had been achieved, and it has been concluded that sufficient control is available to iterate toward unconfined flow at this test condition.

REFERENCES

1. Sears, W.R. "Self-Correcting Wind Tunnels" (The Sixteenth Lanchester Memorial Lecture.) The Aeronautical Journal, Vol. 78, No. 758/759, February/March 1974, pp. 80-89.

2. Erickson, J.C., Jr., and Nenni, J.P. "A Numerical Demonstration of the Establishment of Unconfined-Flow Conditions in a Self-Correcting Wind Tunnel" Calspan Report No. RK-5070-A-1, November 1973.

3. Vidal, R.J., Erickson, J.C., Jr., and Catlin, P.A. "Experiments With a Self-Correcting Wind Tunnel" AGARD CP No. 174 on Wind Tunnel Design and Testing Techniques, October 1975.

4. Sears, W.R., Vidal, R.J., Erickson, J.C., Jr., and Ritter, A. "Inter-ference-Free Wind-Tunnel Flows by Adaptive-Wall Technology" Journal of Aircraft, Vol. 14, No. 11, November 1977, pp. 1042-1050.

5. Vidal, R.J., Catlin, P.A. and Chudyk, D.W. "Two-Dimensional Subsonic Experiments with an NACA 0012 Airfoil" Calspan Report No. RK-5070-A-3, December 1973.

6. Vidal, R.J., and Erickson, J.C., Jr. "Research on Adaptive Wall Wind Tunnels", AEDC Report No. AEDC-TR-78-36, November 1978.

7. Lo, C.F. and Kraft, E.M. "Convergence of the Adaptive-Wall Wind Tunnel" AIAA Journal, Vol. 16, No. 1, January 1978, pp. 67-72.

8. Lo, C.F. and Sickles, W.L. "Analytical and Numerical Investigation of the Convergence of the Adaptive-Wall Concept" AEDC Report No. AEDC-TR-79-55, November 1979.

9. Kraft, E.M. and Parker, R.L., Jr. "Experiments for the Reduction of Wind Tunnel Wall Interference by Adaptive-Wall Technology" AEDC Report No. AEDC-TR-79-51, October 1979.

10. Parker, R.L., Jr. and Sickles, W.L. "Application of Adaptive Wall Tech-niques in a Three-Dimensional Wind Tunnel with Variable Wall Porosity" AIAA Paper No. 80-0157, January 14-16, 1980.

11. Mercer, J.E., Geller, E.W., Johnson, M.L. and Jameson, A. "A Computer Code to Model Swept Wings in an Adaptive Wall Transonic Wind Tunnel" AIAA Paper No. 80-0156, January 14-16, 1980.

12. Murman, E.M., Bailey, F.R. and Johnson, M.L. "TSFOIL-A Computer Code for Two-Dimensional Transonic Calculations, Including Wind-Tunnel Wall Effects and Wave-Drag Evaluation" Paper No. 26 in Aerodynamic Analyses Requiring Advanced Computers, NASA-SP-347-Part 2, March 1975.

13. Sears, W.R. "Small Perturbation Theory", Section C of General Theory of High Speed Aerodynamics, Vol. VI of High Speed Aerodynamics and Jet Propulsion, Princeton U. Press, 1954.

14. Van Dyke, M. Perturbation Methods in Fluid Mechanics, Academic Press, New York, 1964.

15. Churchill, R.V. Complex Variables and Applications, Second Edition, McGraw-Hill, New York, 1960.
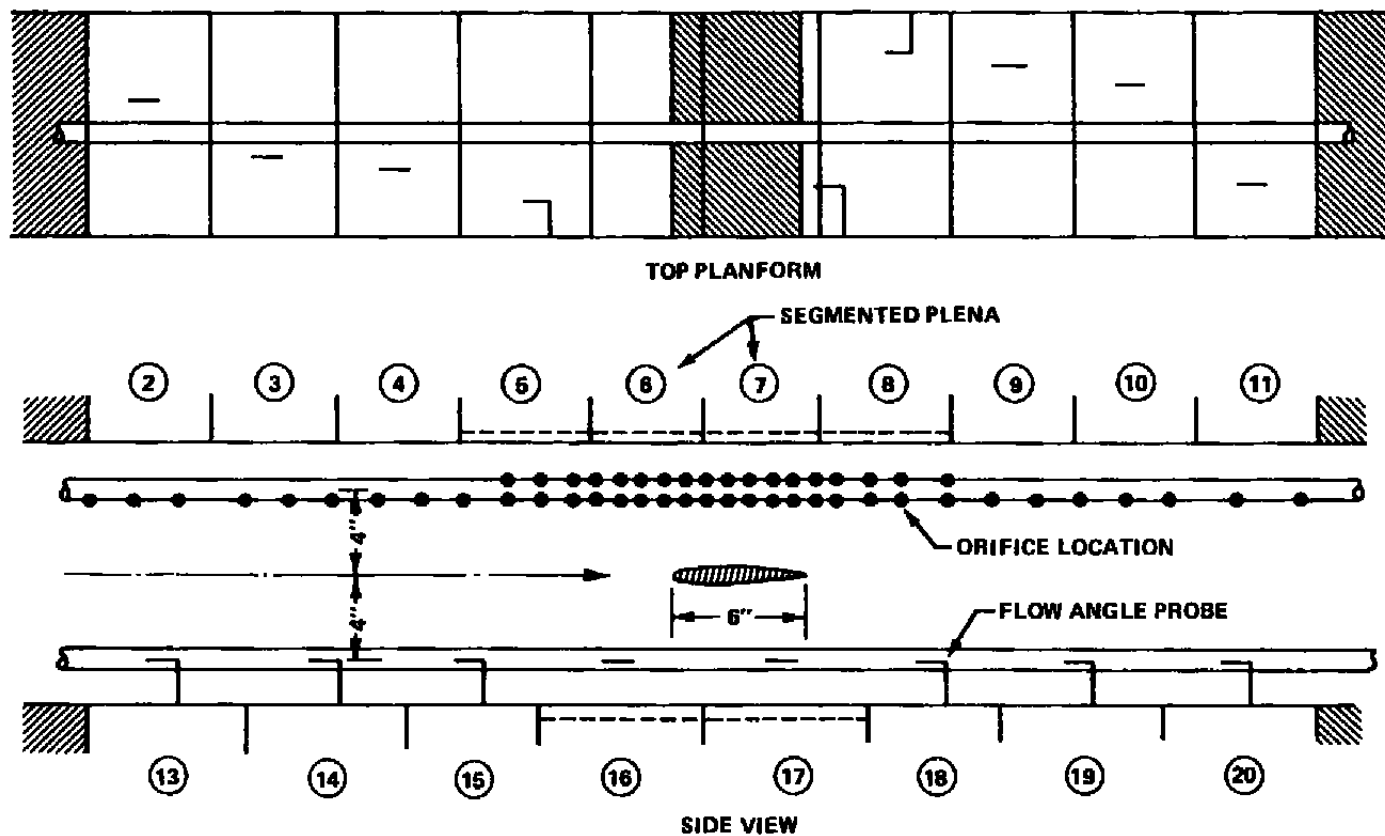
TOP PLANFORM

SIDE VIEW

Figure 1   SCHEMATIC OF STATIC PIPES AND FLOW ANGLE PROBES
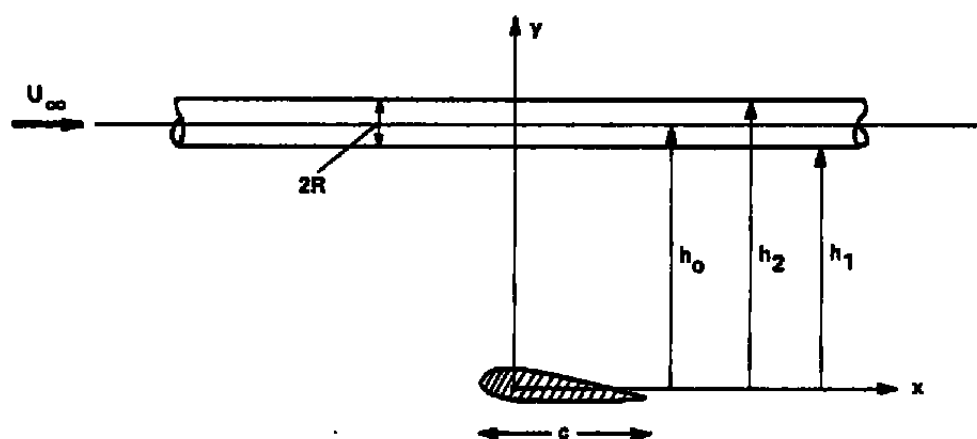
Figure 2   SCHEMATIC OF MODEL AND STATIC PIPE
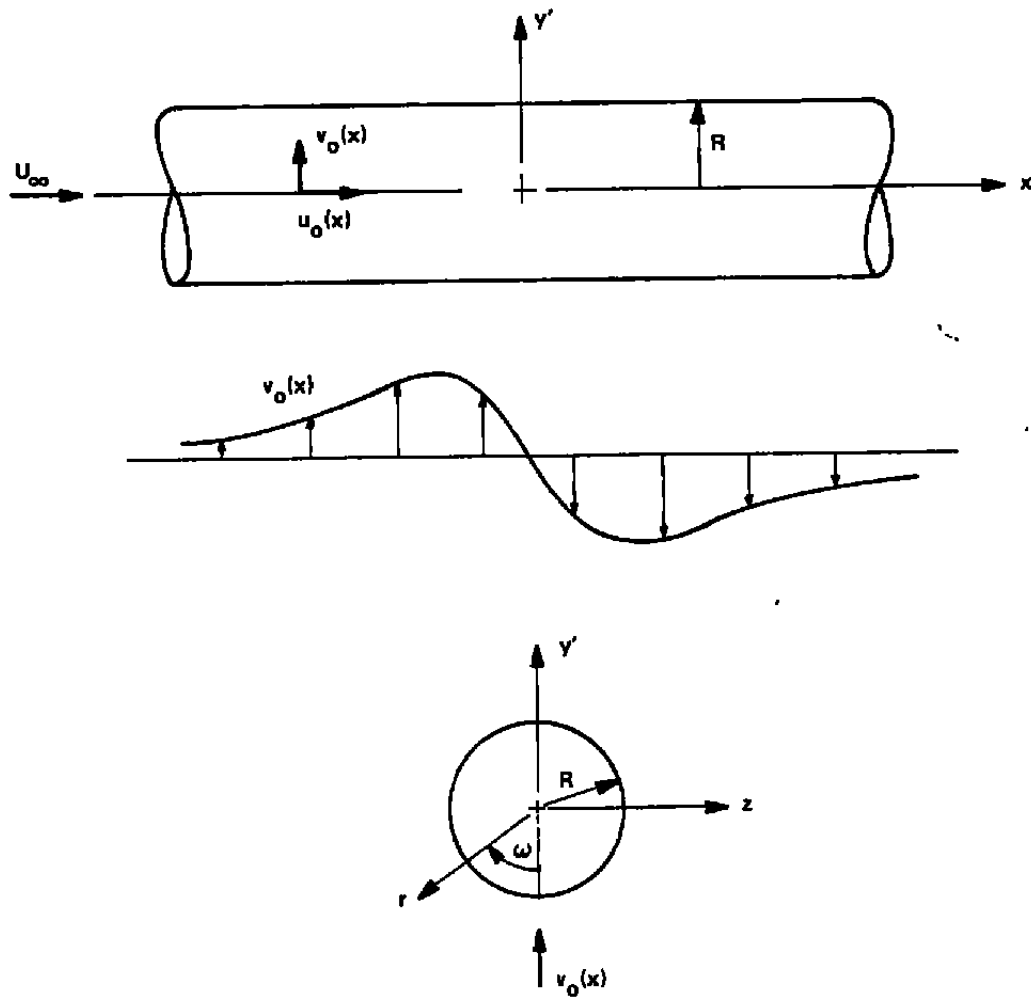
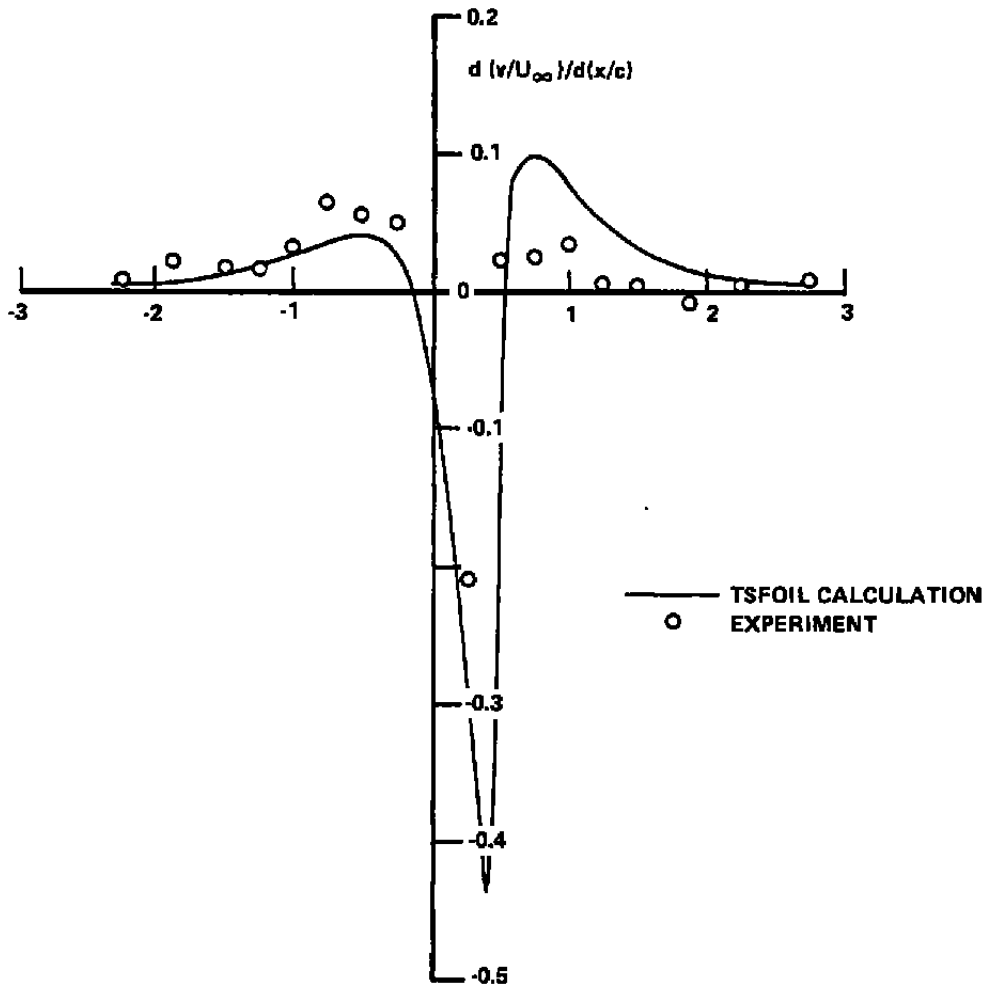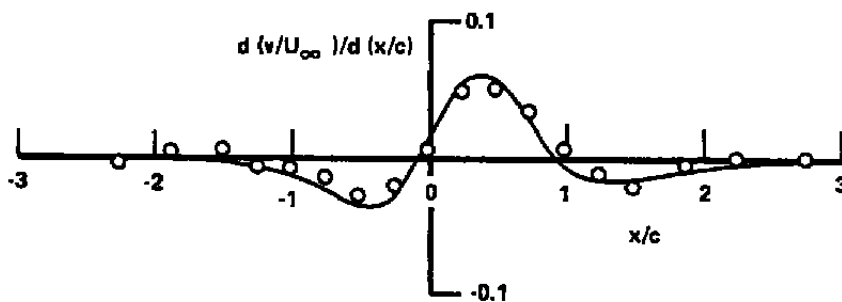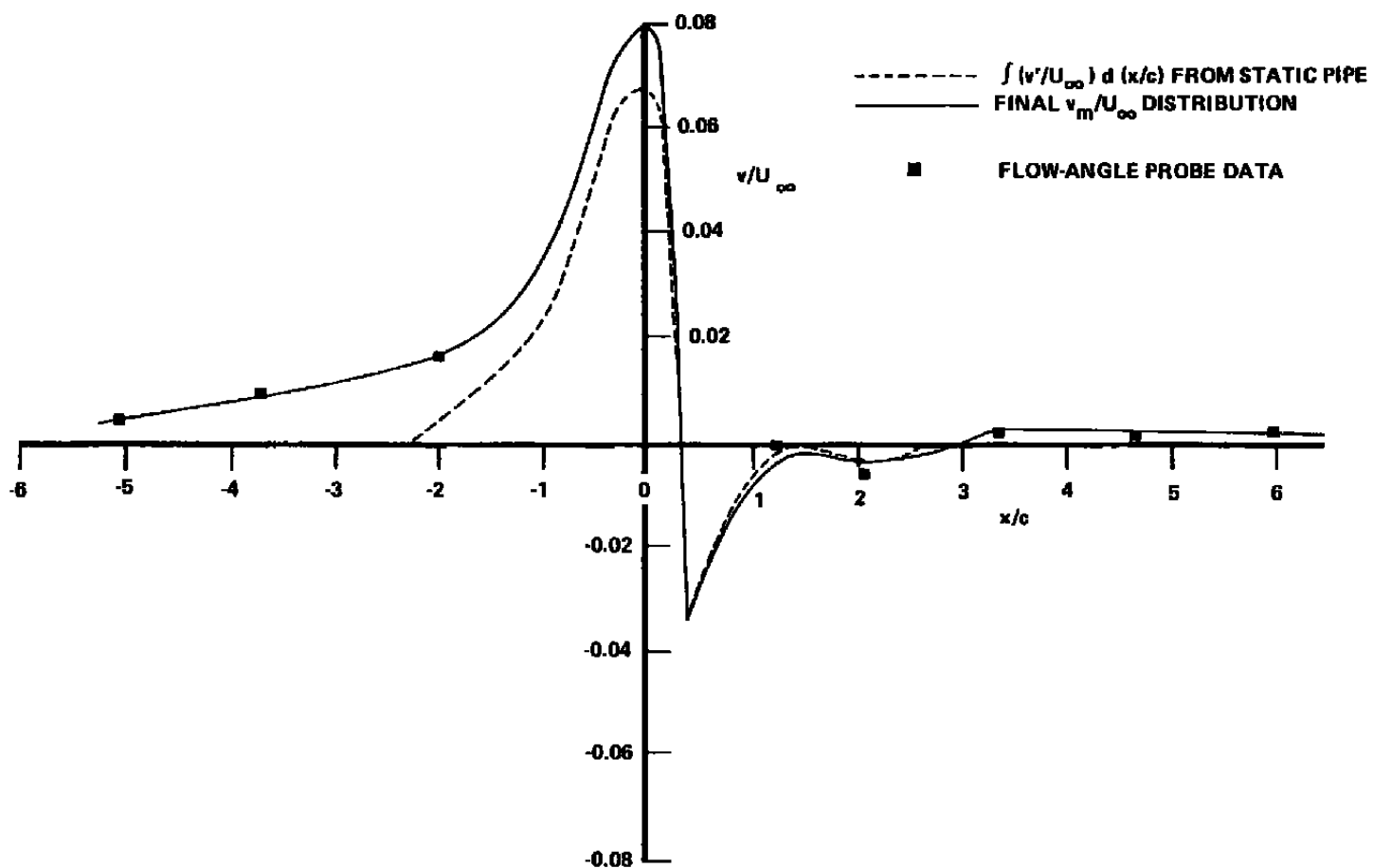Figure 3   MODEL/WALL INDUCED FLOW INCIDENT TO THE STATIC PIPE

(a) UPPER CONTROL SURFACE, h/c = 1.0

(b) LOWER CONTROL SURFACE, h/c = -1.0

Figure 4  STATIC PIPE MEASUREMENTS OF STREAMWISE DERIVATIVE OF NORMAL VELOCITY COMPONENTS, $M_\infty = 0.8$, $\alpha = 4^\circ$, 4% BLOCKAGE, SECOND ITERATIVE STEP

38

(a) UPPER CONTROL SURFACE, h/c = 1.0

Figure 5  NORMAL VELOCITY COMPONENTS DETERMINED FROM STATIC PIPES
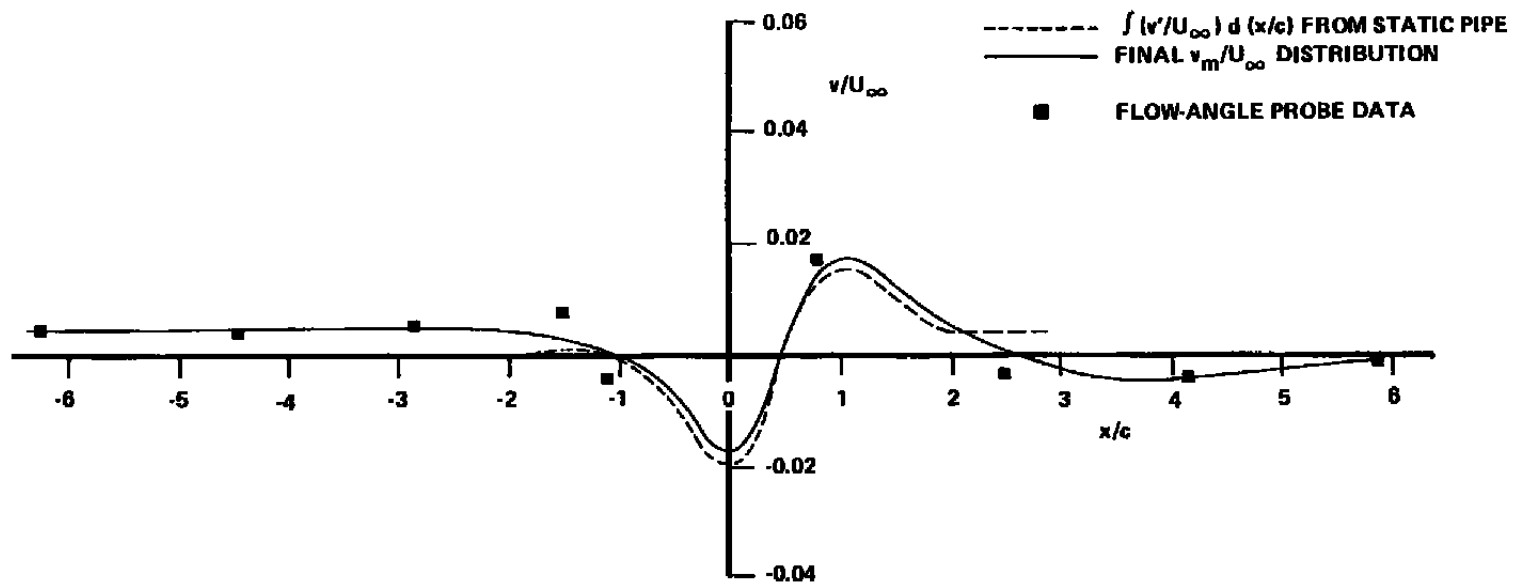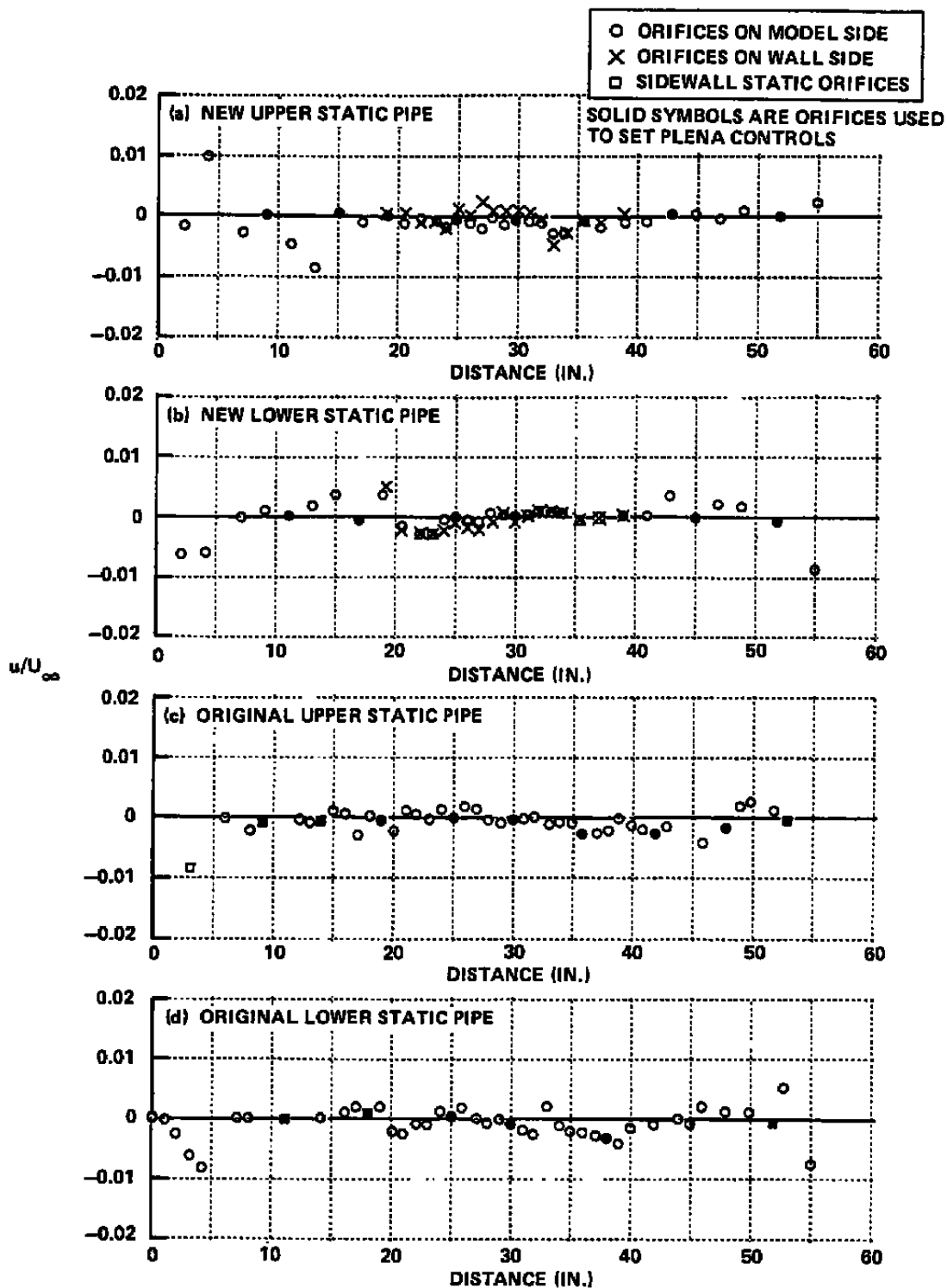AND FLOW-ANGLE PROBES, $M_\infty$ = 0.8, $\alpha$ = 4°, 4% BLOCKAGE, SECOND
ITERATIVE STEP

(b) LOWER CONTROL SURFACE, h/c = -1.0

Figure 5  (Cont.)  NORMAL VELOCITY COMPONENTS DETERMINED FROM STATIC PIPES
AND FLOW-ANGLE PROBES, $M_\infty$ = 0.8,  $\alpha$ = 4°, 4% BLOCKAGE, SECOND
ITERATIVE STEP

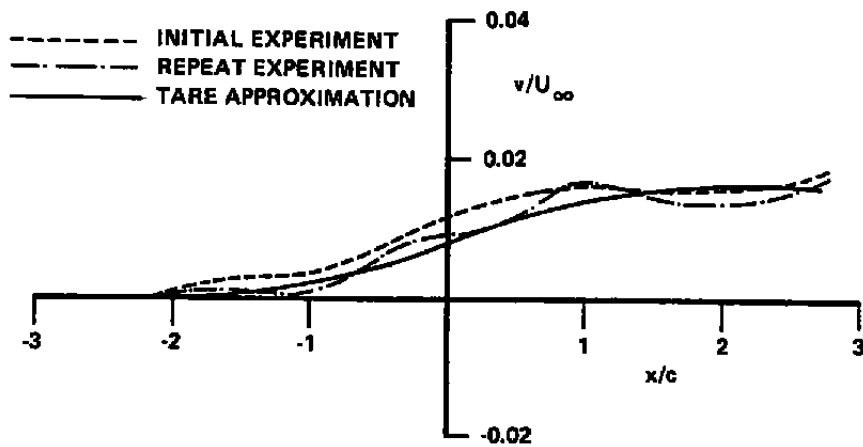Figure 6  VELOCITY DISTRIBUTIONS AT $M_\infty = 0.85$

Figure 7  APPARENT NORMAL VELOCITY COMPONENT MEASURED BY UPPER STATIC
PIPE IN UNIFORM, PARALLEL FLOW WITHOUT MODEL, $M_\infty = 0.8$, $h/c = 1.0$
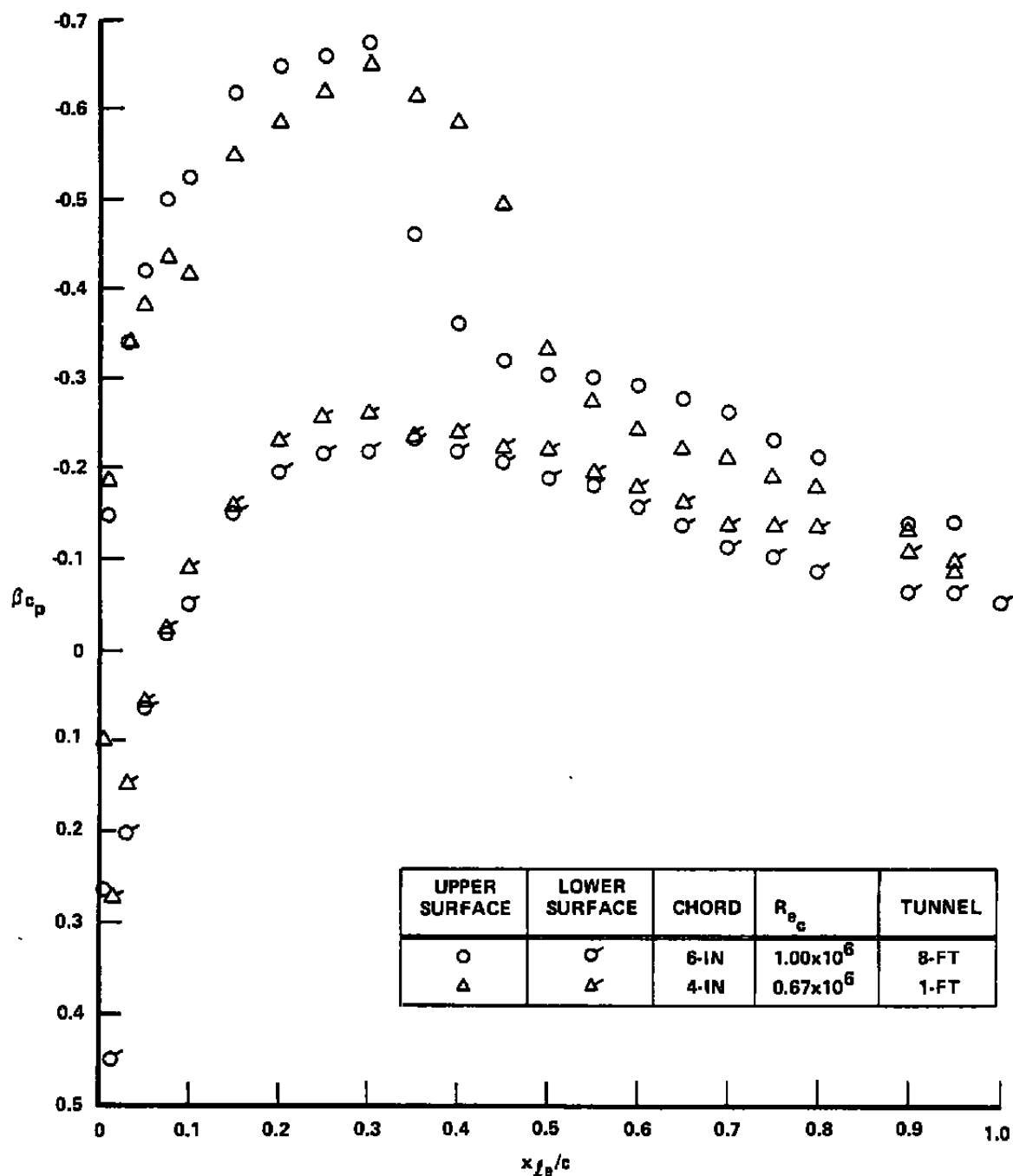
Figure 8   COMPARISON OF MEASURED AIRFOIL PRESSURE DISTRIBUTIONS,
$M_\infty = 0.8$, $\alpha = 4^O$, FIRST ITERATIVE STEP

Figure 9   STREAMWISE DISTURBANCE VELOCITY COMPONENTS, $M_\infty$ = 0.8, $\alpha$ = 4°, 4% BLOCKAGE, FIRST ITERATIVE STEP
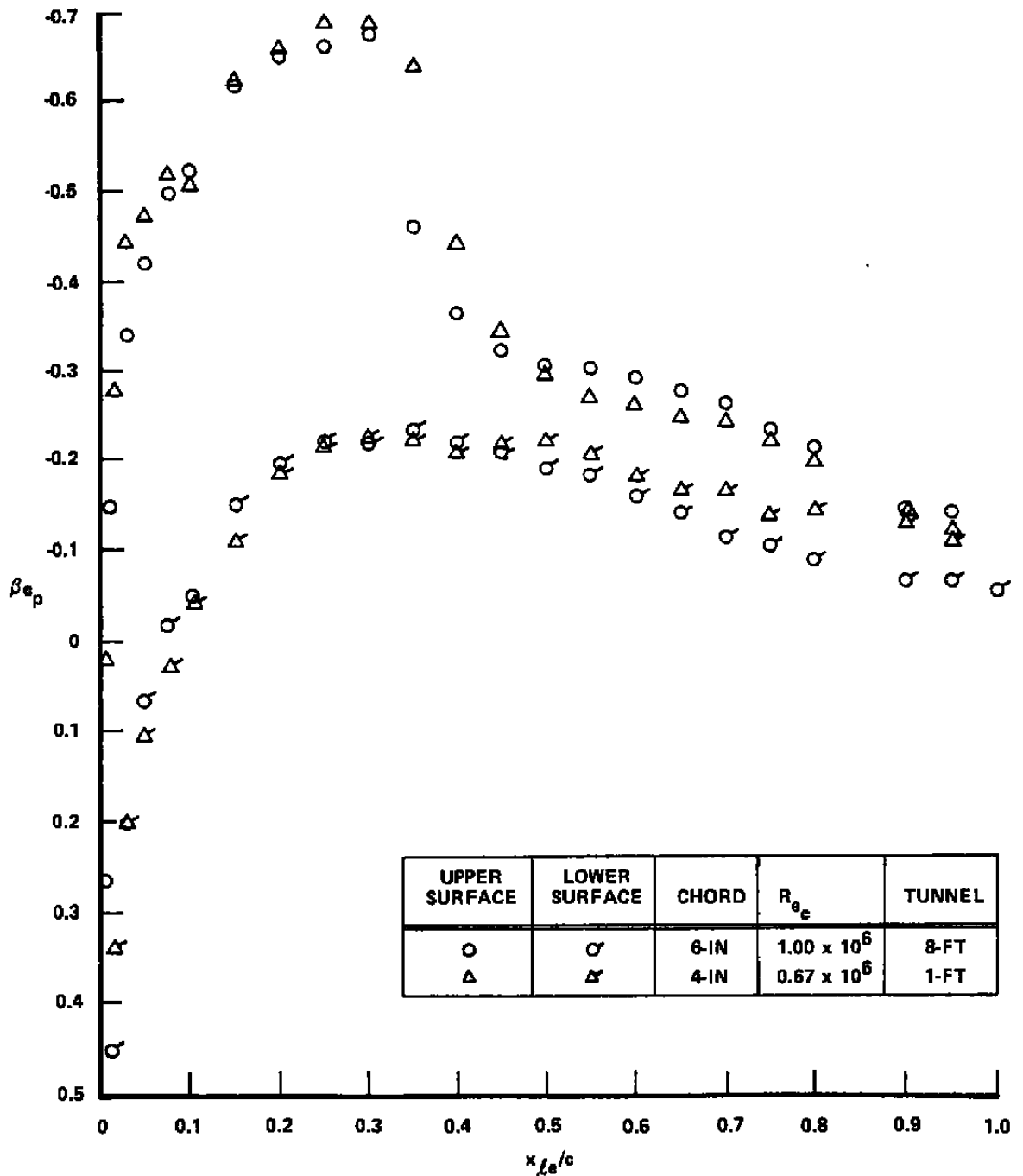
Figure 10   COMPARISON OF MEASURED AIRFOIL PRESSURE DISTRIBUTIONS,
$M_\infty = 0.8$,  $\alpha = 4^\circ$, SECOND ITERATIVE STEP

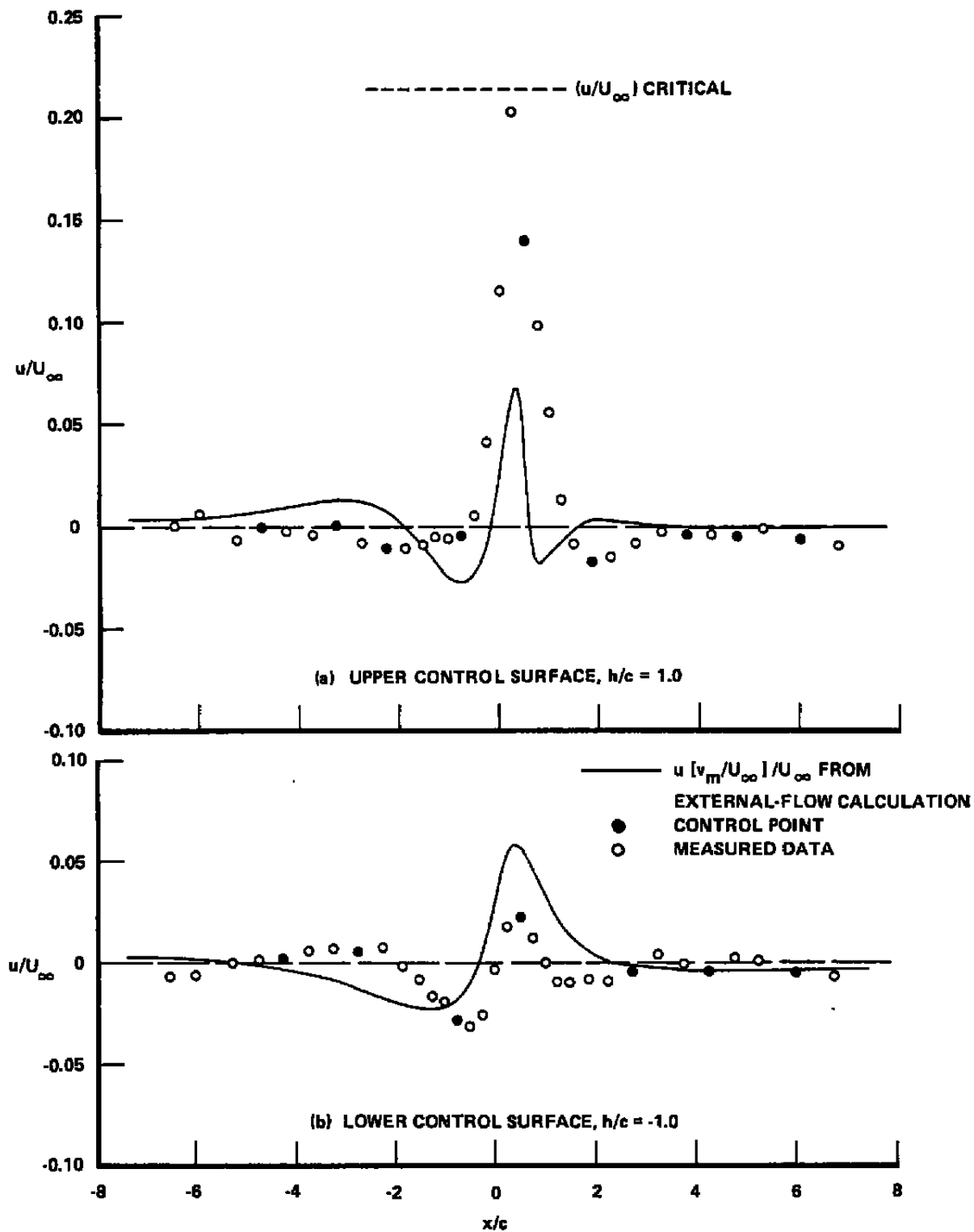| UPPER SURFACE | LOWER SURFACE | CHORD | $R_{e_c}$ | TUNNEL |
|---|---|---|---|---|
| O | O' | 6-IN | $1.00 \times 10^6$ | 8-FT |
| Δ | Δ' | 4-IN | $0.67 \times 10^6$ | 1-FT |

Figure 11  STREAMWISE DISTURBANCE VELOCITY COMPONENTS, $M_\infty = 0.8$, $\alpha = 4°$,
4% BLOCKAGE, SECOND ITERATIVE STEP

46

(a) UPPER CONTROL SURFACE, h/c = 1.0

Figure 12  MEASURED STREAMWISE DISTURBANCE VELOCITY COMPONENTS, $M_\infty$ = 0.9, $\alpha$ = 4°, 4% BLOCKAGE, INITIAL VALVE SETTINGS

(b) LOWER CONTROL SURFACE, h/c = -1.0

Figure 12 (Cont.) MEASURED STREAMWISE DISTURBANCE VELOCITY COMPONENTS, $M_\infty = 0.9$, $\alpha = 4^0$, 4% BLOCKAGE, INITIAL VALVE SETTINGS

(a)  UPPER CONTROL SURFACE, h/c = 1.0

Figure 13   MEASURED STREAMWISE DISTURBANCE VELOCITY COMPONENTS, $M_\infty$ = 0.9, $\alpha$ = 4°, 4% BLOCKAGE, PRELIMINARY VALVE ADJUSTMENTS

(b)  LOWER CONTROL SURFACE, h/c = -1.0

Figure 13 (Cont.)  MEASURED STREAMWISE DISTURBANCE VELOCITY COMPONENTS, $M_\infty$ = 0.9, $\alpha$ = 4°, 4% BLOCKAGE, PRELIMINARY VALVE ADJUSTMENTS
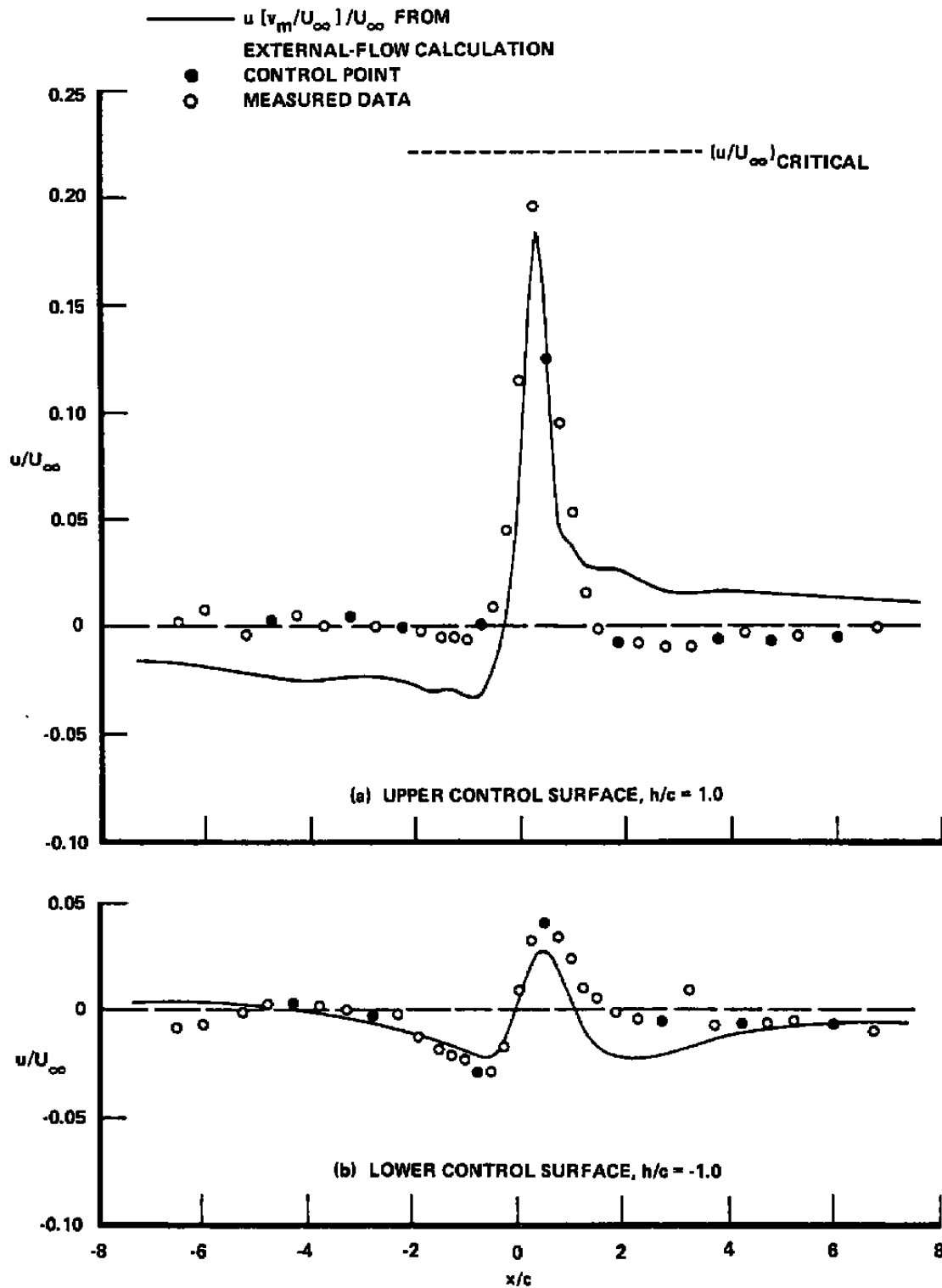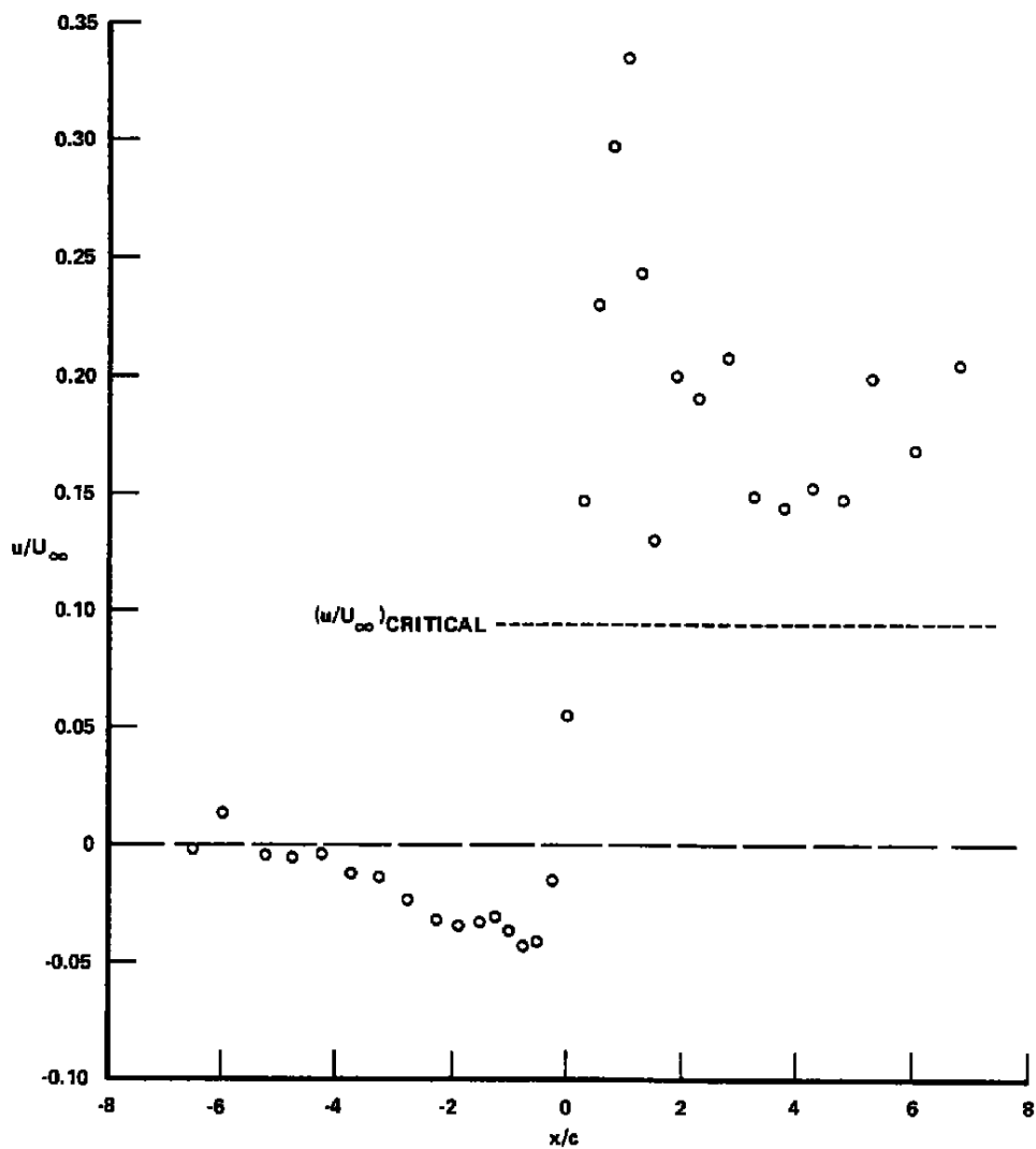
(a) UPPER CONTROL SURFACE, h/c = 1.0
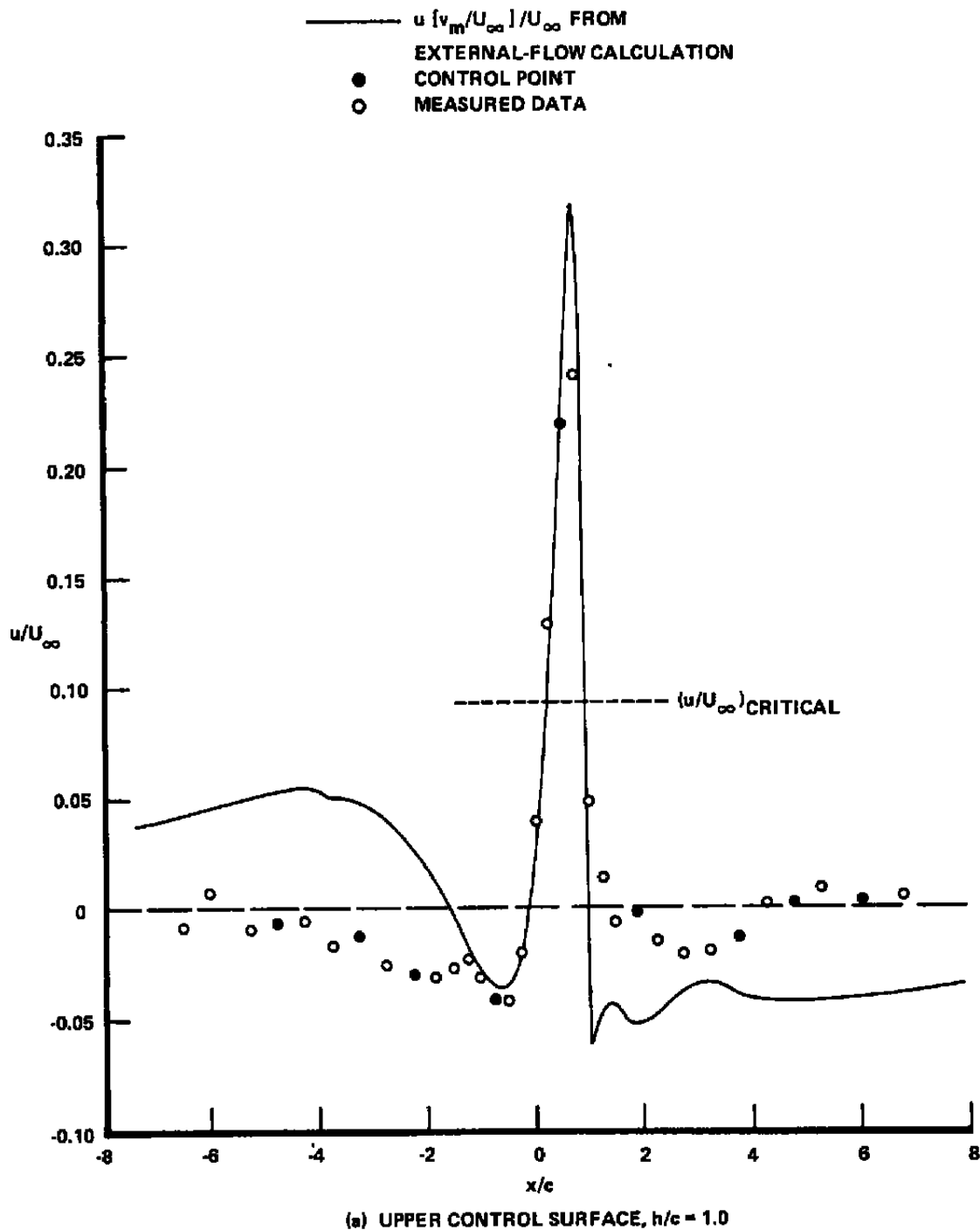
Figure 14   STREAMWISE DISTURBANCE VELOCITY COMPONENTS, $M_\infty$ = 0.9,
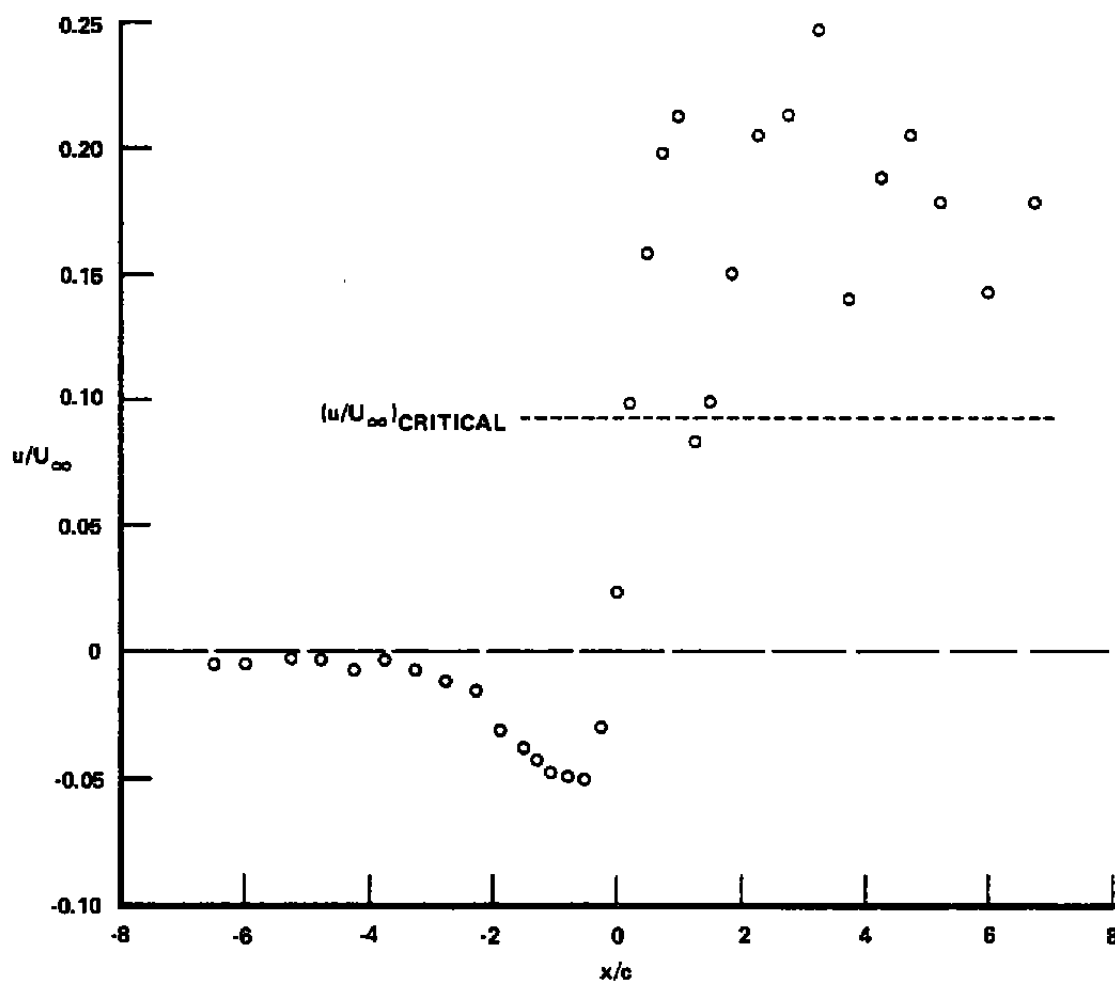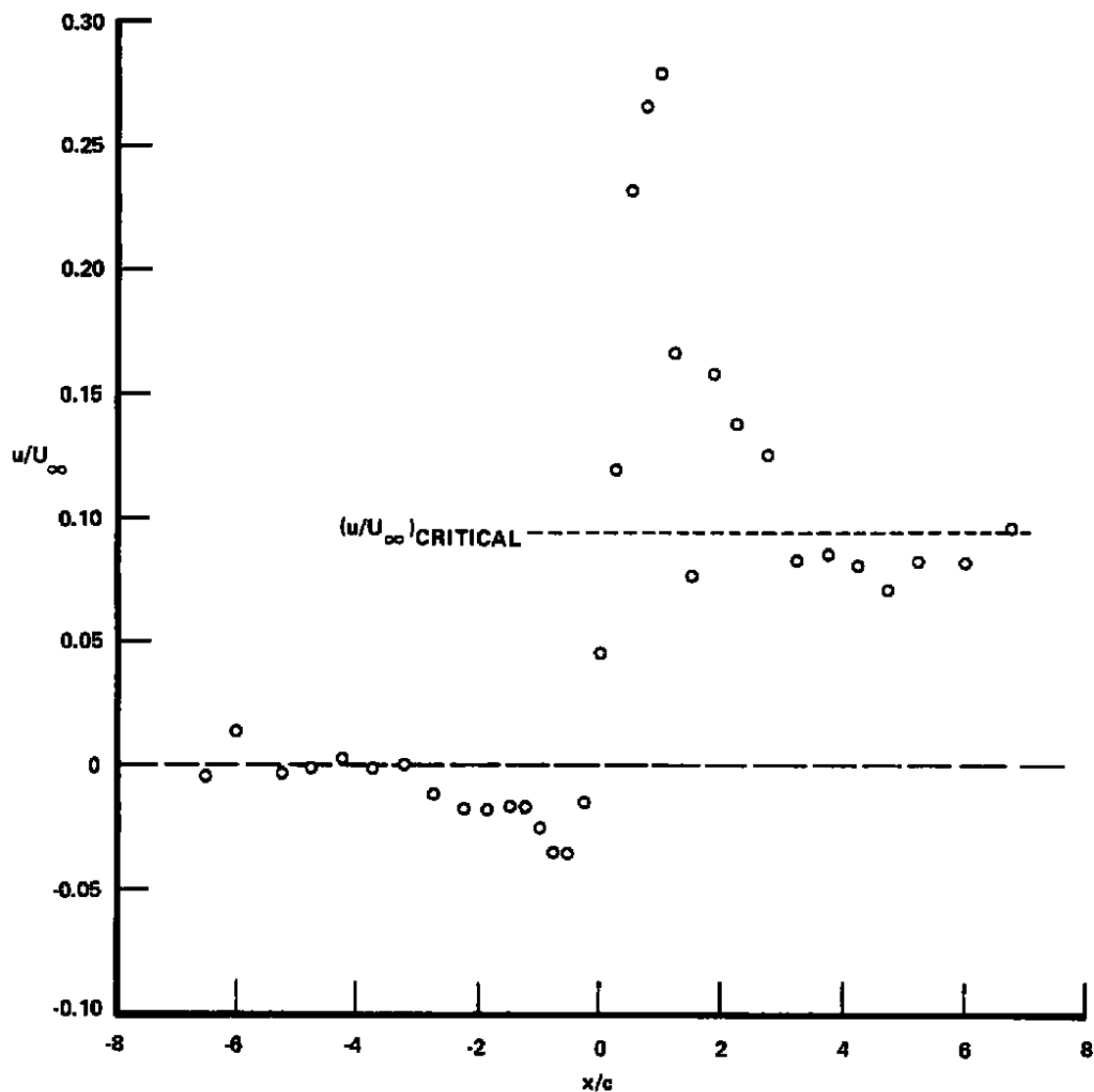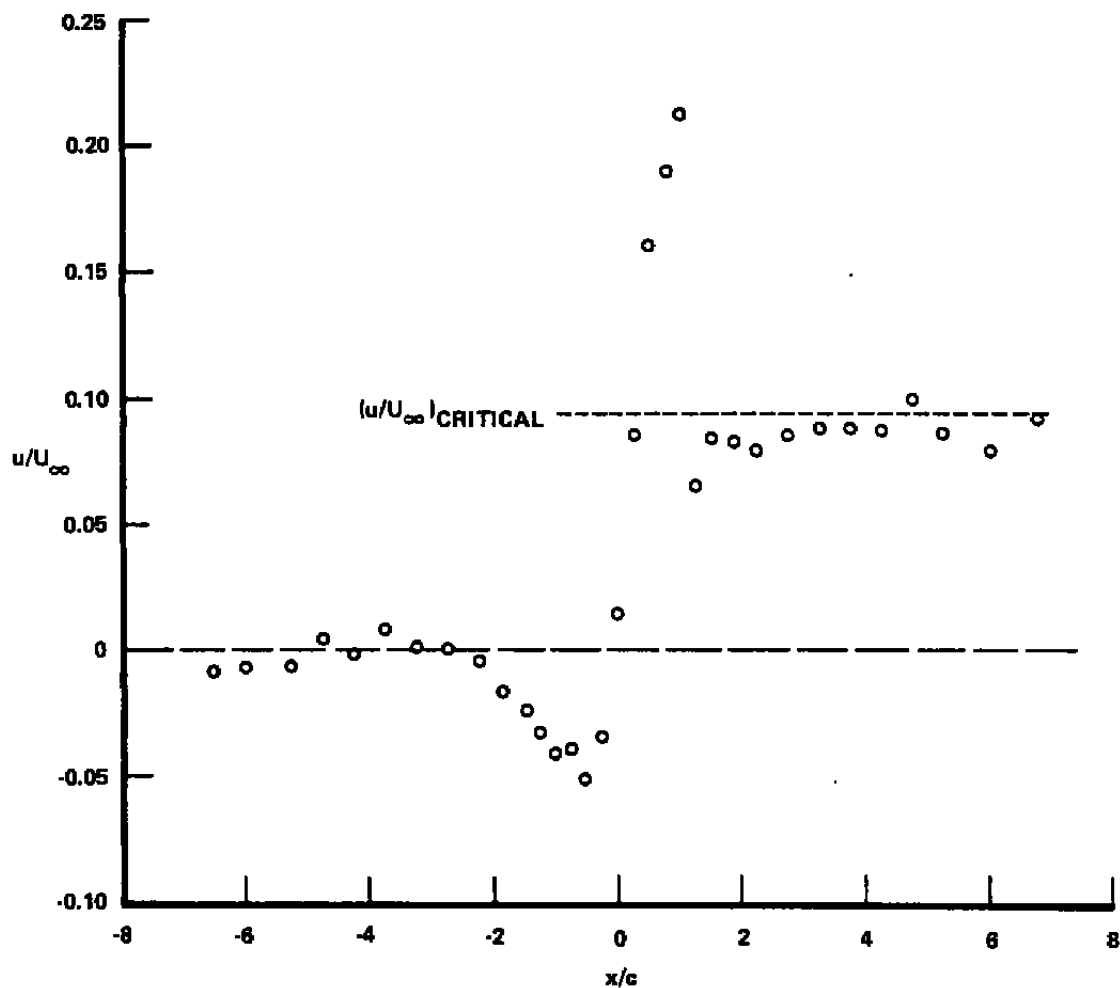$\alpha$ = 4°, 4% BLOCKAGE, FIRST ITERATIVE STEP

51
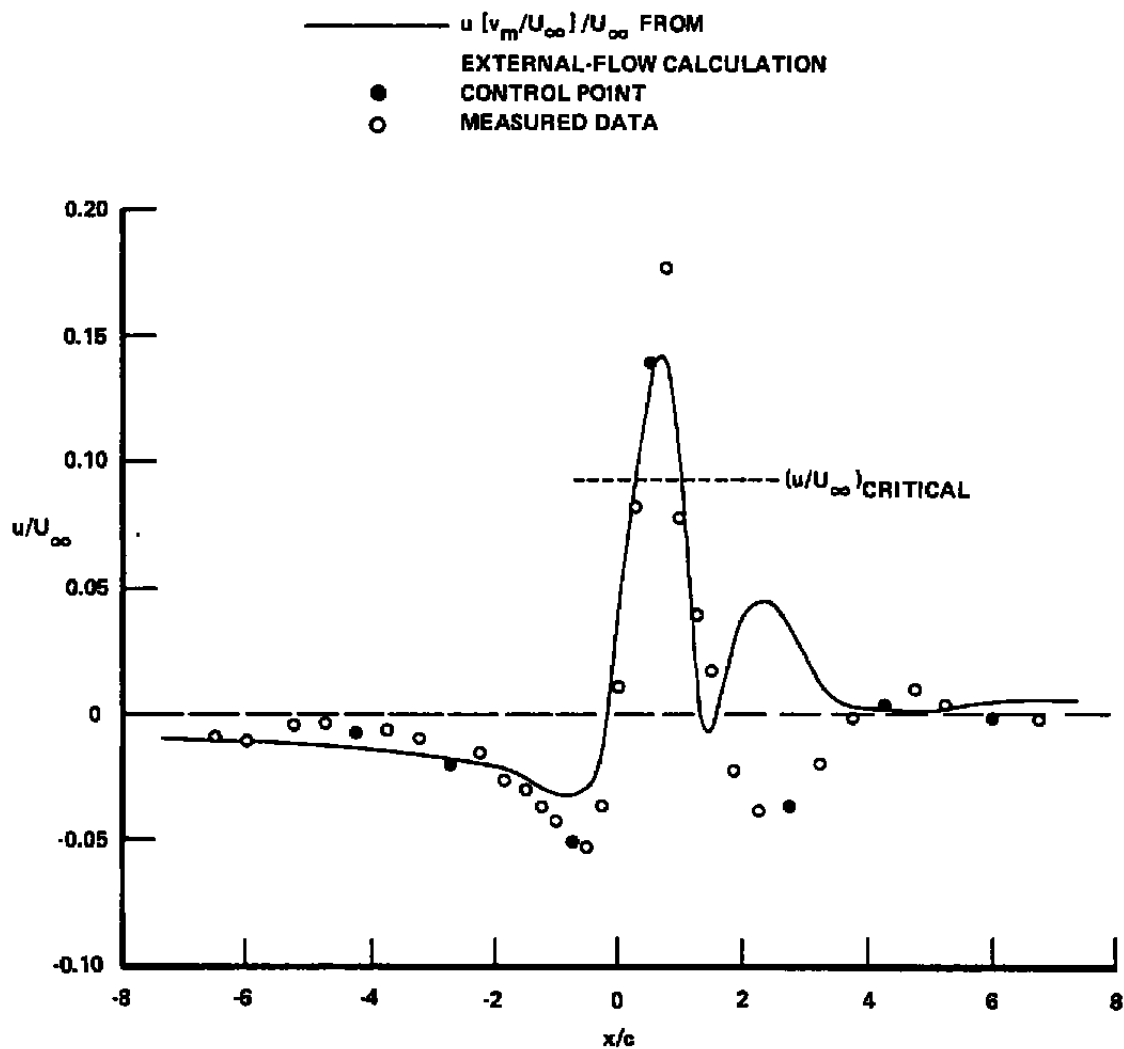
(b) LOWER CONTROL SURFACE, h/c = -1.0

Figure 14 (Cont.) STREAMWISE DISTURBANCE VELOCITY COMPONENTS, $M_\infty$ = 0.9, $\alpha$ = 4°, 4% BLOCKAGE, FIRST ITERATIVE STEP
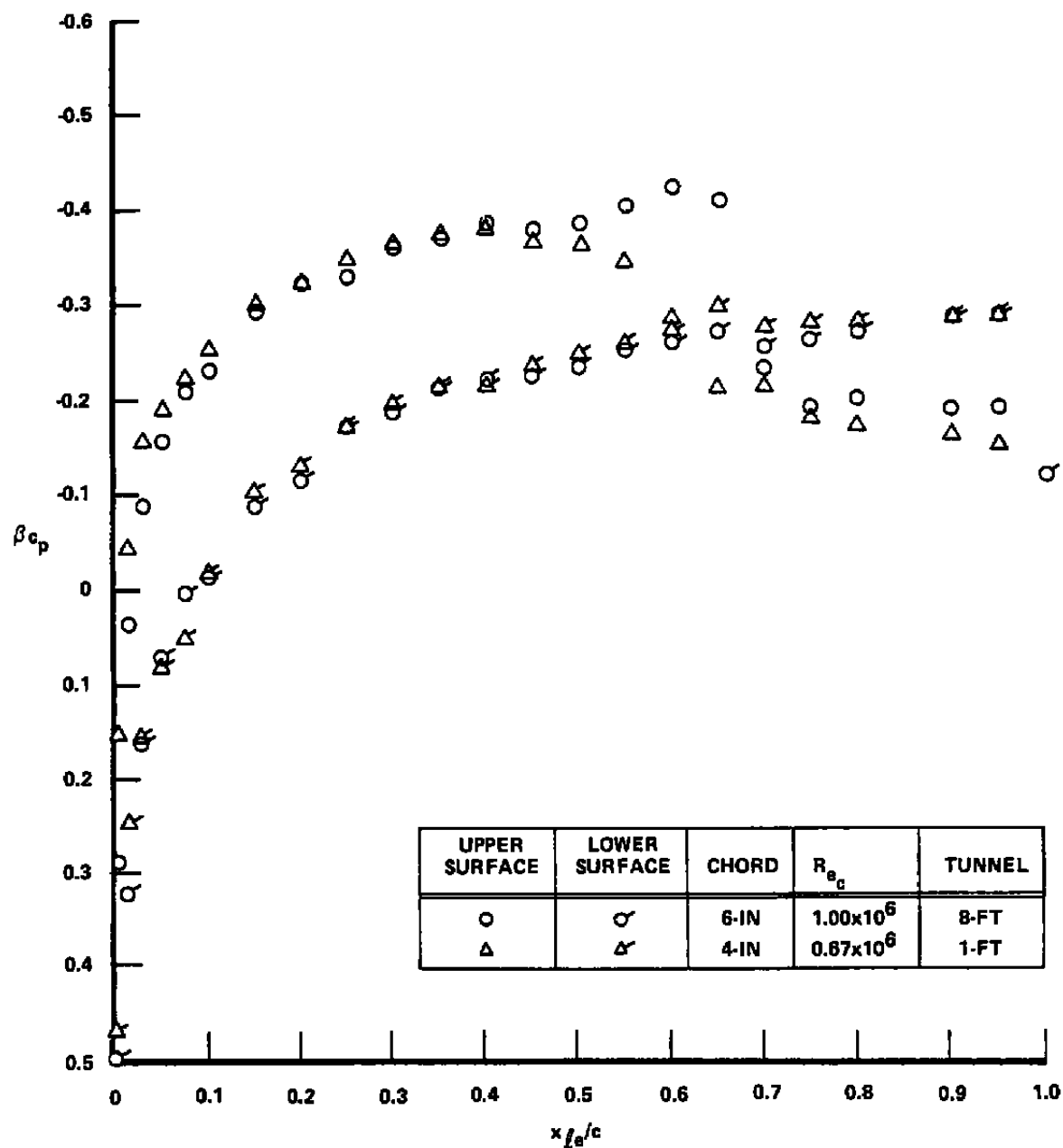
Figure 15   COMPARISON OF MEASURED AIRFOIL PRESSURE DISTRIBUTIONS,
$M_\infty = 0.9$,  $\alpha = 4^0$, FIRST ITERATIVE STEP

TABLE I

EMPTY TUNNEL FLOW MEASUREMENTS OF $u/U_\infty$

| MACH NUMBER | UPPER PIPE | | LOWER PIPE | | BOTH PIPES | |
|---|---|---|---|---|---|---|
| | MEAN | STD. DEV. | MEAN | STD. DEV. | MEAN | STD. DEV. |
| .55 | -0.0017 | ± 0.0016 | -0.0003 | ± 0.0021 | -0.0010 | ±0.0020 |
| .75 | -0.0008 | ±0.0016 | -0.0006 | ± 0.0017 | -0.0007 | ±0.0016 |
| .85 | -0.0008 | ± 0.0025 | -0.0008 | ± 0.0024 | -0.0008 | ±0.0024 |
| .95 | -0.0000 | ± 0.0046 | -0.0014 | ± 0.0036 | -0.0007 | ±0.0042 |

TABLE II

DIFFERENTIAL MEASUREMENTS ACROSS PIPE OF $C_{P_1} - C_{P_2}$

IN EMPTY TUNNEL

| MACH NUMBER | UPPER PIPE | | LOWER PIPE | |
|---|---|---|---|---|
| | MEAN | STD. DEV. | MEAN | STD. DEV. |
| .55 | +0.0004 | ±0.0024 | +0.0008 | ±0.0022 |
| .75 | +0.0014 | ±0.0024 | -0.0010 | ±0.0016 |
| .85 | +0.0014 | ±0.0026 | -0.0010 | ±0.0018 |
| .95 | +0.0016 | ±0.0030 | -0.0012 | ±0.0030 |

APPENDIX


Several features of the static-pipe analysis and applications are presented here. The first is a more rigorous derivation of the static pipe analysis using matched asymptotic expansions. This derivation served to verify that the slender-body analysis in Section 2.3 is correct and consistent to second order. The second is an alternative application of a static pipe in two dimensions and the third is a static-pipe application in a three-dimensional disturbance field.

A.1    STATIC-PIPE ANALYSIS BY MATCHED ASYMPTOTIC EXPANSIONS


The geometry of the flow is given in Figures 2 and 3, as before. Again, the flow is assumed to be subsonic, but compressible, so that the Prandtl-Glauert approximation applies. The total velocity potential $\phi^T(\bar{x}, \bar{q}', \bar{z})$ is of the form

$$\phi^T(\bar{x}, \bar{q}', \bar{z}) = U_\infty \bar{x} + \epsilon U_\infty \left[ \phi_1(\bar{x}, \bar{q}') + \phi_2(\bar{x}, \bar{q}', \bar{z}) \right] \tag{A1}$$

where $\bar{x} = x/c$ , etc. as in the main text, and

$$\phi_1 = \phi^m / U_\infty \epsilon$$

$$\phi_2 = \phi^p / U_\infty \epsilon$$

in terms of the main text notation of Eq. (1), where $\phi^m$ is the two dimensional perturbation potential of the disturbances introduced by the model and wall and $\phi^p$ is the three-dimensional perturbation potential arising from the interaction of the pipe with the model/wall-induced flow field. The surface of the pipe is described by

$$\mathscr{S} = \bar{q}'^2 + \bar{z}^2 - \delta^2 = 0$$

where $\delta = R/c$ , the nondimensional pipe radius. In the Prandtl-Glauert approximation, the potential satisfies

$$(1 - M_\infty^2) \, \phi_{\bar{x}\bar{x}}^T \; + \; \phi_{\bar{q}'\bar{q}'}^T \; + \; \phi_{\bar{z}\bar{z}}^T \; = \; 0 \qquad\qquad (A2)$$

subject to the boundary condition

$$\nabla \phi^T \cdot \nabla \mathcal{S} \; = \; 0 \qquad on \qquad \mathcal{S} = 0 \qquad\qquad (A3)$$

As in the main text, it is assumed that $\delta$ is a small parameter, that is, $\delta \ll 1$, and the technique of matched asymptotic expansions[14] is used to find the appropriate expansion for $\phi_2$. As $\delta \longrightarrow 0$, the pipe shrinks to a line. Tentatively, then, the outer solution is represented by a line doublet distribution plus a line source distribution, viz.

$$\phi^{T,0} \sim U_\infty \, \bar{x} \; + \; \epsilon \, U_\infty \left\{ \phi_1(\bar{x}, \bar{q}') \; + \; \frac{\delta^2}{4\pi} \, \frac{\bar{q}'}{\bar{r}^2} \int_{-\infty}^{\infty} \frac{P(\bar{x}_o)(\bar{x} - \bar{x}_o) \, d\bar{x}_o}{[(\bar{x} - \bar{x}_o)^2 + \beta^2 \bar{r}^2]^{1/2}} \right.$$

$$\left. + \; \frac{\sigma_1(\delta)}{2\pi} \int_{-\infty}^{\infty} \frac{Q(\bar{x}_o) \, d\bar{x}_o}{[(\bar{x} - \bar{x}_o)^2 + \beta^2 \bar{r}^2]^{1/2}} \right\} \qquad\qquad (A4)$$

where $\bar{r}^2 = \bar{q}'^2 + \bar{z}^2$. The doublet strength $P(\bar{x}_o)$ will be determined by matching with an inner solution to first order in $\delta$. The source term (second integral expression) is not needed to first order in $\delta$, so both its strength $Q(\bar{x}_o)$ and gauge function[14] $\sigma_1(\delta)$ will be determined by matching with higher-order inner solutions.

## A.1.1    Inner Solution

The inner problem is obtained by stretching the coordinate normal to the pipe by

$$Y = \bar{q}'/\delta \quad , \quad Z = \bar{z}/\delta$$

---

14.    Van Dyke, M.  Perturbation Methods in Fluid Mechanics,  Academic Press, New York,  1964.

Then $\phi_1(\bar{x}, \bar{y}')$ must be expanded accordingly as

$$\phi_1(\bar{x}, \delta Y) = \phi_{10}(\bar{x}) + \delta \phi_{11}(\bar{x}) Y + \delta^2 \phi_{12}(\bar{x}) Y^2 + O(\delta^3) \qquad (A5)$$

It should be noted that $d\phi_{10}(\bar{x})/d\bar{x}$ is proportional to the desired streamwise disturbance velocity component $u_o$ along the pipe centerline and $\delta \phi_{11}(\bar{x})$ is proportional to the normal component $v_o'$ there.

Next, a total inner solution is assumed of the form

$$\phi^{T,I} \equiv \bar{\phi} = U_\infty \bar{x} + \epsilon U_\infty \left\{ \phi_{10} + \delta (\phi_{11} Y + \bar{\phi}_2) + \delta^2 (\phi_{12} Y^2 + \bar{\phi}_3) \right.$$
$$\left. + O(\delta^3, \delta^3 \ln \delta) \right\} \qquad (A6)$$

It can be shown that both $\bar{\phi}_2$ and $\bar{\phi}_3$ satisfy the two-dimensional Laplace's equation in the crossflow plane, while the boundary condition, Eq. (A3), reduces to

$$2 Y \bar{\phi}_{2_Y} + 2 Z \bar{\phi}_{2_Z} = -2 Y \phi_{11} \qquad (A7)$$

and

$$2 Y \bar{\phi}_{3_Y} + 2 Z \bar{\phi}_{3_Z} = -4 Y^2 \phi_{12} \qquad (A8)$$

both on

$$Y^2 + Z^2 - 1 = 0$$

Physically, it may be seen that the problem for $\bar{\phi}_2$ corresponds to that of a cylinder with unit radius immersed in a flow of magnitude $\phi_{11}$. The corresponding solution is

$$\bar{\phi}_2 = \phi_{11} Y / (Y^2 + Z^2) + G_1(\bar{x}) \qquad (A9)$$

or, in the polar coordinates of Figure 3 ($Y = -R \cos \omega$, $Z = -R \sin \omega$),

$$\bar{\phi}_2 = -\phi_{11} \cos \omega / R + G_1(\bar{x})$$

This equation is of the same form as Eq. (5) in the derivation in the main text. Matching with the outer solution will be carried out in Section A.1.2 to obtain $G_1(\bar{z})$ and $P(\bar{z})$ .

The solution for $\bar{\Phi}_3$ is most easily found using polar coordinates, in terms of which Eq. (A8) becomes

$$\bar{\Phi}_{3_R} = -2\,\phi_{12}\,\cos^2\omega \tag{A11}$$

on $R = 1$, where the subscript $R$ denotes differentiation with respect to $R$. After suitable manipulation, Poisson's integral formula can be used to solve for $\bar{\Phi}_3$ . First, let

$$\bar{\Phi}_3 = \bar{\Phi}_3^B + K\,\ln R + G_2(\bar{z}) \tag{A12}$$

where $K$ is a constant which will be chosen later. Then

$$\bar{\Phi}_{3_R} = \bar{\Phi}_{3_R}^B + \frac{K}{R}$$

and Eq. (A11) becomes

$$-2\,\phi_{12}\,\cos^2\omega = \bar{\Phi}_{3_R}^B\Big|_{R=1} + K$$

or

$$\bar{\Phi}_{3_R}^B\Big|_{R=1} = -(K + 2\,\phi_{12}\,\cos^2\omega)$$

In order to use the Poisson integral formula, $K$ is chosen such that

$$\int_0^{2\pi} \bar{\Phi}_{3_R}^B\Big|_{R=1}\,d\omega = 0$$

which leads to $K = -\phi_{12}$ , so that

$$\bar{\Phi}_{3_R}^B\Big|_{R=1} = \phi_{12}\,(1 - 2\cos^2\omega) \tag{A13}$$

58

Finally, by Poisson's integral formula (see Reference 15, p. 254)

$$\bar{\Phi}_3^{\,\beta} = - \frac{\phi_{12}}{2\pi} \int_0^{2\pi} (1 - 2\cos^2 \omega') \, \ln\left[ 1 - 2R \sin(\omega' - \omega) + R^2 \right] d\omega' \quad \text{(A14)}$$

The function $\bar{\Phi}_3$ is now determined up to a function of $\bar{x}$, $G_2(\bar{x})$ say, and possible eigensolutions that are required to match with the outer solution.

### A.1.2  Matching and Final Solution Forms

The outer solution, Eq. (A4), when written in terms of the inner variables, becomes

$$\phi^{T,0} = U_\infty \bar{x} + \epsilon U_\infty \left\{ \phi_1(\bar{x}, \delta Y) + \frac{\delta}{4\pi} \frac{Y}{R^2} \int_{-\infty}^{\infty} \frac{P(\bar{x}_o)(\bar{x} - \bar{x}_o) \, d\bar{x}_o}{[(\bar{x} - \bar{x}_o)^2 + \delta^2 \beta^2 R^2]^{1/2}} \right.$$
$$\left. + \frac{\sigma_1(\delta)}{2\pi} \int_{-\infty}^{\infty} \frac{Q(\bar{x}_o) \, d\bar{x}_o}{[(\bar{x} - \bar{x}_o)^2 + \delta^2 \beta^2 R^2]^{1/2}} \right\} \quad \text{(A15)}$$

When this equation is expanded for small $\delta$, using Eq. (A5), the result is

$$\phi^{T,0} \sim U_\infty \bar{x} + \epsilon U_\infty \left\{ \phi_{10}(\bar{x}) + \delta \phi_{11}(\bar{x}) Y + \delta^2 \phi_{12}(\bar{x}) Y^2 \right.$$
$$+ \frac{\delta Y}{4\pi R^2} \left[ \int_{-\infty}^{\bar{x}} P(\bar{x}_o) \, d\bar{x}_o - \int_{\bar{x}}^{\infty} P(\bar{x}_o) \, d\bar{x}_o \right] + \frac{\sigma_1(\delta)}{2\pi} \left[ -Q(\bar{x}) \, 2 \ln R \right.$$
$$- Q(\bar{x}) \ln \delta^2 \beta^2 + \int_{-\infty}^{\bar{x}} Q'(\bar{x}_o) \ln 2(\bar{x} - \bar{x}_o) \, d\bar{x}_o$$
$$\left. - \int_{\bar{x}}^{\infty} Q'(\bar{x}_o) \ln 2(\bar{x}_o - \bar{x}) \, d\bar{x}_o \right] + o(\delta^3, \sigma_1(\delta) \delta) \right\} \quad \text{(A16)}$$

15.  Churchill, R.V.  Complex Variables and Applications,  Second Edition, McGraw-Hill, New York, 1960.

The inner solution, Eq. (A6), when written in terms of the outer variables and using the results in Eqs. (A10) and (A14), becomes

$$\bar{\Phi} = U_\infty \bar{x} + \epsilon U_\infty \left\{ \phi_{10} + \left[ \phi_{11} \bar{y}' + \frac{\delta^2 \phi_{11} \bar{y}'}{\bar{r}^2} + \delta G_1(\bar{z}) \right] + \left[ \phi_{12} \bar{y}'^2 \right. \right.$$

$$- \delta^2 \phi_{12} \ln(\bar{r}/\delta) - \frac{\delta^2 \phi_{12}}{2\pi} \int_0^{2\pi} (1 - 2 \cos^2 \omega') \ln \left[ 1 - 2(\bar{r}/\delta) \sin(\omega'-\omega) \right.$$

$$\left. \left. + (\bar{r}/\delta)^2 \right] d\omega' + \delta^2 G_2(\bar{z}) \right] \right\} \tag{A17}$$

When this equation is expanded for small $\delta$, the result is

$$\bar{\Phi} \sim U_\infty \bar{x} + \epsilon U_\infty \left\{ \phi_{10} + \left[ \phi_{11} \bar{y}' + \frac{\delta^2 \phi_{11} \bar{y}'}{\bar{r}^2} + \delta G_1(\bar{z}) \right] \right.$$

$$\left. + \left[ \phi_{12} \bar{y}'^2 - \delta^2 \phi_{12} \ln(\bar{r}/\delta) + \delta^2 G_2(\bar{z}) \right] + O(\delta^4) \right\} \tag{A18}$$

Matching Eqs. (A16) and (A18) results in

$$G_1(\bar{z}) = 0$$
$$P(\bar{z}) = 2\pi \phi_{11}'(\bar{z})$$

to complete the solution for the line doublet distribution, and

$$\sigma_1(\delta) = \delta^2$$

$$Q(\bar{z}) = \pi \phi_{12}(\bar{z})$$

$$G_2(\bar{z}) = - \phi_{12}(\bar{z}) \ln \delta\beta + \frac{1}{2} \int_{-\infty}^{\bar{z}} \phi_{12}'(\bar{z}_o) \ln 2(\bar{z}-\bar{z}_o) d\bar{z}_o$$

$$- \frac{1}{2} \int_{\bar{z}}^{\infty} \phi_{12}'(\bar{z}_o) \ln 2(\bar{z}_o-\bar{z}) d\bar{z}_o$$

to complete the solution for the line source distribution. Inspection of the first term of $G_2(\bar{z})$ indicates that an additional term of order $\delta^2 \ln \delta$ should have been assumed in the inner expansion of Eq. (A6). However, consideration of the boundary conditions quickly shows that this additional term is a function only of $\bar{x}$ which is precisely this portion of $G_2(\bar{z})$. Furthermore, no eigensolutions are necessary to perform the matching.

### A.1.3    Pressure Coefficient

The pressure coefficient may be calculated from the inner solution and to second order in the small parameters, i.e., retaining $\epsilon^2$, $\delta^2$ and $\epsilon\delta$, is

$$C_P = -2\epsilon\,\phi_{10}' - 2\epsilon\delta\,(\phi_{11}'\,Y + \Phi_{2\bar{z}}) - \epsilon^2\left[(\phi_{10}')^2(1-M_\infty^2)\right.$$

$$\left. +\ \Phi_{2\bar{z}} + (\phi_{11} + \Phi_{2_Y})^2\right] \tag{A19}$$

On the pipe at $\omega = 0$ and $\pi$,

$$C_{P_1} = -2\epsilon\,\phi_{10}' + 4\epsilon\delta\,\phi_{11}' - \epsilon^2(\phi_{10}')^2(1-M_\infty^2) \tag{A20}$$

$$C_{P_2} = -2\epsilon\,\phi_{10}' - 4\epsilon\delta\,\phi_{11}' - \epsilon^2(\phi_{10}')^2(1-M_\infty^2) \tag{A21}$$

In terms of the physical quantities, these equations become

$$C_{P_1} = -2\hat{u}_o(\bar{z}) + 4\delta\,\hat{v}_o'(\bar{z}) - \beta^2\hat{u}_o^2(\bar{z}) \tag{A22}$$

$$C_{P_2} = -2\hat{u}_o(\bar{z}) - 4\delta\,\hat{v}_o'(\bar{z}) - \beta^2\hat{u}_o^2(\bar{z}) \tag{A23}$$

which are the same as had been derived in the main text.

### A.2    ALTERNATIVE TWO-DIMENSIONAL STATIC-PIPE APPLICATIONS

The static-pipe response analyzed in Section 2.3 and Appendix A.1 can be exploited to determine $v_o(z)$ directly without the necessity for a separate, independent probe measurement to determine the constant of integration in Eq. (29) of the main text. This alternative procedure would involve a different pipe configuration from the ones that were fabricated. In particular, a third set of pressure measurements must be made with each pipe, either by a third row of orifices or by rotation of the pipe.

This procedure can be described in terms of Eqs. (22) to (24) of the main text, which give the pressure coefficients on the pipe at $\omega = 0$, $\pi/2$ and $\pi$, called $C_{P_1}$, $C_{P_0}$ and $C_{P_2}$, respectively. These equations are

$$C_{P_1} \equiv C_P(\bar{x}, 0) = -2\,\hat{u}_o(\bar{x}) - \beta^2\,\hat{u}_o^2(\bar{x}) + 4\,\delta\,\hat{v}_o'(\bar{x}) \tag{A24}$$

$$C_{P_o} \equiv C_P(\bar{x}, \tfrac{\pi}{2}) = -2\,\hat{u}_o(\bar{x}) - \beta^2\,\hat{u}_o^2(\bar{x}) - 4\,\hat{v}_o^2(\bar{x}) \tag{A25}$$

$$C_{P_2} \equiv C_P(\bar{x}, \pi) = -2\,\hat{u}_o(\bar{x}) - \beta^2\,\hat{u}_o^2(\bar{x}) - 4\,\delta\,\hat{v}_o'(\bar{x}) \tag{A26}$$

It should be noted that alternatively, $C_{P_o} = C_P(\bar{x}, 3\pi/2)$, since the results for $\omega = \pi/2$ and $3\pi/2$ must be equal by symmetry. If Eqs. (A24) and (A26) are added and subtracted, Eqs. (25), (26) and (28) of the main text are obtained, namely

$$\frac{C_{P_1} + C_{P_2}}{4} = -\hat{u}_o(\bar{x}) - \frac{\beta^2\,\hat{u}_o^2(\bar{x})}{2} \tag{A27}$$

which when solved for $\hat{u}_o$, gives

$$\hat{u}_o(x) = -\frac{1}{\beta^2}\left\{1 - \left[1 - \frac{\beta^2(C_{P_1} + C_{P_2})}{2}\right]^{1/2}\right\} \tag{A28}$$

and

$$\hat{v}_o'(\bar{x}) = \frac{C_{P_1} - C_{P_2}}{8\,\delta} \tag{A29}$$

If Eqs. (A25) and (A27) are combined, $\hat{v}_o^2(\bar{x})$ is found directly, namely

$$\hat{v}_o^2(\bar{x}) = \frac{C_{P_1} + C_{P_2}}{8} - \frac{C_{P_o}}{4} \tag{A30}$$

Therefore, by making the three sets of measurements of $C_{P_o}$, $C_{P_1}$ and $C_{P_2}$, $\hat{u}_o(\bar{x})$ can be found directly from Eq. (A28), $\hat{v}_o'(\bar{x})$ from Eq. (A29) and $\hat{v}_o^2(\bar{x})$ from Eq. (A30). Finally, $\hat{v}_o(\bar{x})$ can be found from

$$\hat{v}_o(\bar{x}) = \sqrt{\hat{v}_o^2(\bar{x})}\;\; sgn\left\{\left[d\,\hat{v}_o^2(\bar{x})\,/\,d\bar{x}\right]\,/\,\hat{v}_o'(\bar{x})\right\} \tag{A31}$$

where the signum function is

$$\text{sgn } x = \begin{cases} -1 & , & x < 0 \\ 0 & , & x = 0 \\ 1 & , & x > 0 \end{cases} \qquad (A32)$$

In principle, it would only be necessary to measure $C_{P_o}$ at a sufficient number of points so that $\hat{v}_o^2(\bar{z})$ and its derivative could be determined accurately for evaluation of $\hat{v}_o(\bar{z})$ by Eq. (A31) at a single point, say $\bar{x}_o$. Once $\hat{v}_o(\bar{x}_o)$ is known, Eq. (A29) can be integrated as in Eq. (29) of the main text to obtain $\hat{v}_o(\bar{z})$ over the entire interval for which $\hat{v}_o'(\bar{z})$ has been measured. If additional $C_{P_o}$ measurements are made, the accuracy of the entire scheme can be assessed by comparing the results for $\hat{v}_o(\bar{z})$ as determined by Eq. (A31) with those found by integrating Eq. (A29).

## A.3    STATIC-PIPE APPLICATIONS IN THREE-DIMENSIONAL FLOWS

The $y'$ and $z$ components of the three-dimensional flow that is incident to the pipe are shown in the sketch, where both $v_o(x)$ and $w_o(x)$, and so $V_o(x)$ and $\omega_1(x)$ are arbitrary functions of $x$. The relationships among these quantities are

$$v_o(x) = V_o(x) \cos \omega_1(x) \qquad (A33)$$

$$w_o(x) = V_o(x) \sin \omega_1(x) \qquad (A34)$$

$$V_o^2(x) = v_o^2(x) + w_o^2(x) \qquad (A35)$$



63
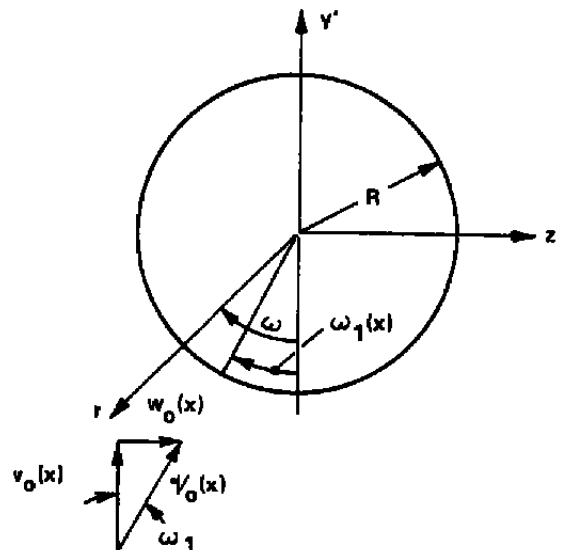
The analysis given in the main text can be adapted readily to this configuration. In particular, the potential for the crossflow in Eq. (5) is replaced by

$$\phi^P(x, y, z) = -\mathcal{V}_o(x) R^2 \cos[\omega - \omega_1(x)] / r \qquad (A36)$$

whereupon Eqs. (6) to (8) are replaced by

$$v_x^P(x, r, \omega) = (-R/r) d\left\{\mathcal{V}_o(x) \cos[\omega - \omega_1(x)]\right\} / dx \qquad (A37)$$

$$v_r^P(x, r, \omega) = \mathcal{V}_o(x) R^2 \cos[\omega - \omega_1(x)] / r^2 \qquad (A38)$$

$$v_\omega^P(x, r, \omega) = \mathcal{V}_o(x) R^2 \sin[\omega - \omega_1(x)] / r^2 \qquad (A39)$$

If the analysis is followed through exactly as in the main text, Eq. (21) is replaced by

$$C_P(\bar{x}, \omega) = -2\hat{u}_o(\bar{x}) - \beta^2 \hat{u}_o^2(\bar{x}) + 4\delta d\left\{\hat{\mathcal{V}}_o(\bar{x}) \cos[\omega - \omega_1(\bar{x})]\right\} / d\bar{x}$$

$$- 4\hat{\mathcal{V}}_o^2(\bar{x}) \sin^2[\omega - \omega_1(\bar{x})] \qquad (A40)$$

or, equivalently, using Eqs. (A33) and (A34),

$$C_P(\bar{x}, \omega) = -2\hat{u}_o(\bar{x}) - \beta^2 \hat{u}_o^2(\bar{x}) + 4\delta d[\hat{v}_o(\bar{x}) \cos\omega + \hat{\omega}_o(x) \sin\omega] / d\bar{x}$$

$$- 4[\hat{v}_o(\bar{x}) \sin\omega - \hat{\omega}_o(\bar{x}) \cos\omega]^2 \qquad (A41)$$

Measurements must be made every 90° around the pipe for three-dimensional flows, either by four rows of static pressure orifices or by a lesser number of rows and pipe rotation. For measurements at $\omega = 0, \pi, \pi/2$ and $3\pi/2$, it follows that

$$C_{P_1} \equiv C_P(\bar{x}, 0) = -2\hat{u}_o(\bar{x}) - \beta^2 \hat{u}_o^2(\bar{x}) + 4\delta \hat{v}_o'(\bar{x}) - 4\hat{\omega}_o^2(\bar{x}) \qquad (A42)$$

$$C_{P_2} \equiv C_P(\bar{x}, \pi) = -2\hat{u}_o(\bar{x}) - \beta^2 \hat{u}_o^2(\bar{x}) - 4\delta \hat{v}_o'(\bar{x}) - 4\hat{\omega}_o^2(\bar{x}) \qquad (A43)$$

$$C_{P_3} \equiv C_P\left(\bar{x}, \frac{\pi}{2}\right) = -2\hat{u}_o(\bar{z}) - \beta^2 \hat{u}_o^2(\bar{z}) + 4\delta\hat{\omega}_o'(\bar{z}) - 4\bar{v}_o^2(\bar{z}) \quad \text{(A44)}$$

$$C_{P_4} \equiv C_P\left(x, \frac{3\pi}{2}\right) = -2\hat{u}_o(\bar{z}) - \beta^2 \hat{u}_o^2(\bar{z}) - 4\delta\hat{\omega}_o'(\bar{z}) - 4\bar{v}_o^2(\bar{z}) \quad \text{(A45)}$$

Adding all four of these, and using Eq. (A35),

$$\hat{u}_o(\bar{z}) + \frac{\beta^2 \hat{u}_o^2(\bar{z})}{2} = -\frac{C_{P_1} + C_{P_2} + C_{P_3} + C_{P_4}}{8} - \hat{v}_o^2(\bar{z}) \quad \text{(A46)}$$

which can be solved for $\hat{u}_o(\bar{z})$ to give

$$\hat{u}_o(\bar{z}) = -\frac{1}{\beta^2}\left\{1 - \left[1 - \frac{\beta^2(C_{P_1} + C_{P_2} + C_{P_3} + C_{P_4})}{4} - 2\beta^2 \hat{v}_o^2(\bar{z})\right]^{1/2}\right\} \quad \text{(A47)}$$

Subtracting $C_{P_2}$ from $C_{P_1}$ and then $C_{P_4}$ from $C_{P_3}$ give, respectively,

$$\hat{v}_o'(\bar{z}) = \frac{C_{P_1} - C_{P_2}}{8\delta} \quad \text{(A48)}$$

$$\hat{\omega}_o'(\bar{z}) = \frac{C_{P_3} - C_{P_4}}{8\delta} \quad \text{(A49)}$$

In addition, the $\hat{u}_o(\bar{z})$, $\hat{v}_o'(\bar{z})$ and $\hat{\omega}_o'(\bar{z})$ terms can be eliminated from Eqs. (A42) to (A45) to give

$$\hat{\omega}_o^2(\bar{z}) = \hat{v}_o^2(\bar{z}) + \frac{C_{P_3} + C_{P_4}}{8} - \frac{C_{P_1} + C_{P_2}}{8} \quad \text{(A50)}$$

With the relationships of Eqs. (A47) to (A50), then, if measurements of all four pressures are made along the pipe, and at least one independent measurement of either $\hat{v}_o(\bar{z})$ or $\hat{\omega}_o(\bar{z})$ is made, say by a probe, all of the desired velocity components can be determined. For example, if $\hat{v}_o(\bar{z})$ is measured independently, Eq. (A48), which is identical with the two-dimensional equation, can be integrated according to Eq. (29) of the main text to give $\hat{v}_o(\bar{z})$. Then Eq. (A50) can be solved for $\hat{\omega}_o^2(\bar{z})$, which in turn can be solved for $\hat{\omega}_o(\bar{z})$, using Eq. (A49), by

$$\hat{\omega}_o(\bar{z}) = \sqrt{\hat{\omega}_o^2(\bar{z})} \, sgn\left\{\left[d\,\hat{\omega}_o^2(\bar{z})/d\bar{z}\right] \middle/ \hat{\omega}_o'(\bar{z})\right\} \quad \text{(A51)}$$

where sgn $\mathcal{X}$ is defined in Eq. (A32). Finally, $\hat{\mathcal{V}}_o^2(\bar{\mathcal{X}})$ can be found from Eq. (A35) whereupon $\hat{u}_o(\bar{\mathcal{X}})$ can be found from Eq. (A47). As an alternative, of course, $\widehat{\omega}_o(\bar{\mathcal{X}}_o)$ could be measured independently and a similar procedure followed to determine the distributions of $\widehat{\omega}_o(\bar{\mathcal{X}})$, $\hat{v}_o^2(\bar{\mathcal{X}})$, $\hat{v}_o(\bar{\mathcal{X}})$, $\hat{\mathcal{V}}_o(\bar{\mathcal{X}})$ and $\mathcal{Q}_o(\bar{\mathcal{X}})$.

NOMENCLATURE

$C_p$      pressure coefficient, $(p - p_\infty)/q_\infty$

$c$      airfoil chord

$G_1, G_2$      functions in definitions of $\bar{\Phi}_2$ and $\bar{\Phi}_3$, Eqs. (A9) and (A12), respectively

$h$      height of static pipe above tunnel centerline, Figure 2

$K$      constant in definition of $\bar{\Phi}_3$, Eq. (A12)

$k$      iterative relaxation factor, Eq. (30)

$M$      Mach number

$P$      doublet strength in outer solution for $\phi$, Eq. (A4)

$p$      static pressure

$Q$      source strength in outer solution for $\phi$, Eq. (A4)

$q_\infty$      free-stream dynamic pressure, $\rho_\infty U_\infty^2/2$

$\mathcal{R}$      nondimensional radius, $r/R$

$R$      static pipe radius, Figures 2 and 3

$Re_c$      Reynolds number based on airfoil chord

$r$      radial coordinate, Figure 3

$s$      function describing surface of static pipe

$sgn$      signum function, Eq. (A32)

$U_\infty$      free-stream velocity

$u, v, \omega$      disturbance velocity components in $x$, $y$, $z$ directions, respectively

$u_{Critical}$      value of $u$ for which $U_\infty + u$ corresponds to $M = 1$

$u \, [v_m / U_\infty] / U_\infty$      nondimensional $u$ found from external-flow calculation

$v_o$      three-dimensional velocity normal to static pipe, Eq. (A35)

$v_o'$      $d\,v_o / d\,x$

$v_x, v_r, v_\omega$      disturbance velocity components in $x$, $r$, $\omega$ directions, respectively, Figure 3

$x, y$      rectangular coordinates with origin at tunnel centerline and $y$ axis coincident with line between junctions between plenum chambers 6 and 7 and 16 and 17, Figures 1 and 2

$x_{\ell e}$      coordinate from airfoil leading edge

$x_o$      reference value of $x$ for determination of $v_o'(x_o)$ in Eq. (29)

$Y, Z$      nondimensional coordinates $y'/\delta$ and $z/\delta$, respectively

$y'$      coordinate from static pipe centerline equal to $y - h_o$, Figures 2 and 3 and Eq. (2)

$z$      static pipe coordinate, Figure 3

$\alpha$      airfoil angle of attack

$\beta$      $\sqrt{1 - M_\infty^2}$

$\delta$      nondimensional static pipe radius, $R/c$

$\epsilon$      parameter representing magnitude of model/wall-induced disturbances due to thickness or angle of attack

$\rho$      air density

$\sigma_1$          gauge function in outer solution for $\phi$ , Eq. (A4)

$\tau$          airfoil thickness-to-chord ratio

$\bar{\Phi}$          inner solution velocity potential, Eq. (A6)

$\bar{\Phi}_2 , \bar{\Phi}_3$     terms in series expansion of $\bar{\Phi}$ , Eq. (A6)

$\bar{\Phi}_3^s$          function in definition of $\bar{\Phi}_3$ , Eqs. (A12) and (A14)

$\phi$          perturbation velocity potential

$\phi_1 , \phi_2$     functions in expansion of $\phi^\tau$ , Eq. (A1)

$\phi_{10} , \phi_{11} , \phi_{12}$  functions in expansion of $\phi_1$ , Eq. (A5)

$\omega$          angular variable in cylindrical coordinate system, Figure 3

$\omega_1$          angular orientation of three-dimensional disturbance flow
          incident to static pipe, Appendix A.3

$\nabla$          gradient operator


SUPERSCRIPTS

$m$          model/wall induced quantity

$p$          static pipe induced quantity

$T$          total quantity

$T,I$          total inner solution quantity

$T,O$          total outer solution quantity

$(1),(2)$          iterative step number

$(ii)$          calculated distribution before relaxation to take second
          iterative step

$\wedge$   nondimensionalization of velocity through division by $U_\infty$

$\sim$   nondimensionalization of length through division by $C$

SUBSCRIPTS

$m$   measured quantity

$o$   quantity at static pipe centerline

$1,2,3,4$   quantity at bottom, top, left-hand side and right-hand side, respectively, of static pipe; $\omega = 0, \pi, \pi/2$ and $3\pi/2$, respectively, in Figure 3

$\infty$   free-stream quantity